Biomedicine & Pharmacotherapy 175 (2024) 116676

Contents lists available at ScienceDirect

Biomedicine & Pharmacotherapy

journal homepage: www.elsevier.com/locate/biopha

Nature-inspired substituted 3-(imidazol-2-yl) morpholines targeting human topoisomerase IIα: Dynophore-derived discovery

Barbara Herlah [a,b], Matej Janežič [a], Iza Ogris [a,c], Simona Golič Grdadolnik [a], Katja Kološa [d], Sonja Žabkar [d], Bojana Žegura [d], Andrej Perdih [a,b,*]

[a] National Institute of Chemistry, Hajdrihova 19, Ljubljana SI 1000, Slovenia
[b] University of Ljubljana, Faculty of Pharmacy, Aškerčeva 7, Ljubljana SI 1000, Slovenia
[c] University of Ljubljana, Faculty of Medicine, Vrazov trg 2, Ljubljana SI 1000, Slovenia
[d] National institute of Biology, Department of Genetic Toxicology and Cancer Biology, Večna pot 121, Ljubljana SI 1000, Slovenia

ARTICLE INFO

Keywords:
Topoisomerase II
Catalytic inhibitors
Chemotherapy
DNA damage
Cancer

ABSTRACT

The molecular nanomachine, human DNA topoisomerase IIα, plays a crucial role in replication, transcription, and recombination by catalyzing topological changes in the DNA, rendering it an optimal target for cancer chemotherapy. Current clinical topoisomerase II poisons often cause secondary tumors as side effects due to the accumulation of double-strand breaks in the DNA, spurring the development of catalytic inhibitors. Here, we used a dynamic pharmacophore approach to develop catalytic inhibitors targeting the ATP binding site of human DNA topoisomerase IIα. Our screening of a library of nature-inspired compounds led to the discovery of a class of 3-(imidazol-2-yl) morpholines as potent catalytic inhibitors that bind to the ATPase domain. Further experimental and computational studies identified hit compound **17**, which exhibited selectivity against the human DNA topoisomerase IIα versus human protein kinases, cytotoxicity against several human cancer cells, and did not induce DNA double-strand breaks, making it distinct from clinical topoisomerase II poisons. This study integrates an innovative natural product-inspired chemistry and successful implementation of a molecular design strategy that incorporates a dynamic component of ligand-target molecular recognition, with comprehensive experimental characterization leading to hit compounds with potential impact on the development of more efficient chemotherapies.

1. Introduction

Type IIA topoisomerases are molecular machines that modulate DNA topology and enable cell replication and the expression of genetic information as well as chromosome segregation [1,2]. Using ATP and Mg^{2+} ions, they cleave two strands of bound DNA (G-segment) to allow the passage of the second DNA (T-segment), thus simplifying the DNA topology [3–6]. Mammalian type II DNA topoisomerase is expressed in two isoforms: α and β. They share a high sequence identity of approximately 70 %, but are differentially expressed in cells; the α isoform is mainly expressed in actively dividing cells and at elevated levels in tumor cells, whereas the β isoform is constitutively expressed [7–9]. Therefore, the α-isoform of topo II is more relevant for the treatment of proliferative diseases such as cancer, although cross-inhibition of the topo IIβ isoform can also be beneficial in some cases [10,11].

Structurally, human DNA topoisomerase IIα (topo IIα) is a large enzyme consisting of two homodimers that are functionally divided into three gates: the N-gate, which consist of two opposing ATPase domains (Fig. 1), the DNA-gate, where cleavage of the bound DNA G-segment occurs, and the C-gate [4,12]. Each ATPase domain also consists of the GHKL (Gyrase, Hsp90, Histidine Kinase, MutL) and transducer domains, which transmit information to the DNA-gate [13]. The crystal structures of the ATPase dimer with a bound ADP and non-hydrolysable ATP ligands [14,15] and a cryo-EM structure of a fully catalytic form of topo IIα provide an atomistic insight into the conformational landscape and dynamics of this enzyme and its catalytic cycle [16].

Due to the crucial role of type II topoisomerases in the normal functioning and survival of cells, these molecular motors have become established targets for cancer chemotherapy [17]. To overcome the limitations of clinically used topoisomerase II poisons [18], such as doxorubicin and etoposide, efforts have been made in the investigation of a new paradigm of catalytic inhibition of topo IIα targeting the ATP

* Correspondence to: National Institute of Chemistry, Hajdrihova 19, Ljubljana SI-1001, Slovenia.
E-mail address: andrej.perdih@ki.si (A. Perdih).

https://doi.org/10.1016/j.biopha.2024.116676
Received 12 March 2024; Received in revised form 22 April 2024; Accepted 29 April 2024
Available online 20 May 2024

binding site [19]. Such compounds could potentially lead to safer chemotherapeutics, as they could circumvent the induction of DNA double-strand breaks (DSBs) caused by clinically used topo II poisons that lead to the formation of secondary tumors and cytotoxicity [20,21]. So far, we have discovered several promising catalytic inhibitors by using various computational molecular design approaches [22–24].

Current strategies for molecular design aim to incorporate the dynamic aspects of ligand-target molecular recognition, understanding the limitations of traditional methods such as molecular docking and pharmacophore models [25,26]. These limitations primarily stem from an incomplete sampling of the conformational landscape and an oversimplified determination of the binding free energy [27,28]. Over the past decade, molecular simulations have emerged as a tool for augmenting the drug discovery process by enabling a more comprehensive exploration of the molecular recognition phenomena [29]. These simulations include various techniques, including binding/unbinding simulations, residence time determination, and free energy calculations [30,31,33]. Among such methods, molecular simulations have been integrated with pharmacophore models to create dynamic pharmacophore models (i.e., dynophores) that represent a fully automated fusion of 3D pharmacophores and molecular dynamics simulations and provide statistical insights into the spatial and temporal occurrence of pharmacophore features [27].

The selection of molecular libraries for molecular design is another important factor. In this respect, natural products, characterized by their scaffold diversity and structural complexity, allow the exploration of a broader chemical space compared to synthetic compounds. They play an important role in drug discovery, especially in infectious diseases and cancer [34–37]. A recent analysis of drugs approved by the US Food and Drug Administration between 1946 and 2019 revealed that 64.9 % of all small molecule anticancer drugs, i.e., 904 of 1394, were natural products or direct derivatives of natural products [35,38,39]. Natural compounds are usually subject to further optimization as they tend to have a higher molecular mass, a larger number of sp^3 carbon and oxygen atoms, more chiral centers, and a higher number of hydrogen bond acceptors and donors compared to synthetic compounds [37,40–43]. To somewhat bridge the gap, nature-inspired synthetic compound libraries are being developed, which, as the name implies, are the product of chemists mining natural libraries for inspiration and often require the development of new or adaptation of existing synthetic strategies [37,44].

In our previous research, we used human topoisomerase IIα as a model target to develop a dynophore-based approach for virtual screening. Using molecular simulations, we derived two dynophore models, one for our discovered catalytic inhibitor from the class of 4,6-substituted 1,3,5-triazin-2(1*H*)-ones [83] and the other for ATP, both bound in the ATP binding site of topo IIα. These models were merged into a joint dynophore-based pharmacophore model that was used in virtual screening with a natural product library (Fig. 1). Experimental validation identified novel flavonoids that catalytically inhibited of topoisomerase IIα and confirmed binding to its ATPase domain. In the absence of a complex crystal structure, a computational analysis confirmed the alignment of the binding model with the original dynophore-based screening model and experimental data [45]. Overall, given the known topo IIα inhibitory properties of these natural products [46,47], this study served as a proof-of-principle for the strategy, which can be generalized and applied to molecular design for various biomolecular systems (Fig. 1) [45].

In this study, we aimed to utilize the validated dynophore-based method to discover catalytic inhibitors targeting the ATP binding site of DNA topoisomerase IIα. Our approach was to refine the dynophore-based pharmacophore model to better map the ATP binding site of this specific topoisomerase. For virtual screening, instead of conventional synthetic small molecule libraries, we used nature-inspired libraries derived from natural product syntheses, combining nature's inventiveness with a chemist's rationality. We first identified 3-(imidazol-2-yl)morpholine hits and then performed extensive mechanistic studies to elucidate the structure activity relationship (SAR) and its effect on topoisomerase IIα in order to expand this chemical class. Through extensive experimental characterization such as testing on human cancer cell lines and additional biochemical and computational experiments, we identified the most favorable lead compounds with (i) a well evaluated mechanism of action on topoisomerase IIα, (ii) selectivity for the human DNA topoisomerase IIα ATPase versus human protein kinases, and (iii) promising toxicity that is mechanistically distinct from conventional topoisomerase II poisons.

2. Results and discussion

2.1. Dynophore-based virtual screening: targeting the ATP binding site of human topoisomerase IIα

First, we reanalyzed the ATP binding site of topoisomerase IIα for design ideas that we could apply to our dynophore-based pharmacophore model to refine it (Figure S1). When visualizing the ATPase dimer of topo IIα using the Computed Atlas of Surface Topology of proteins (CASTp) [48], we observed two cavities within the ATP binding pocket; the first located above and the second below the adenine ring (Fig. 2A), [49]. It has already been established that many of the known ATPases

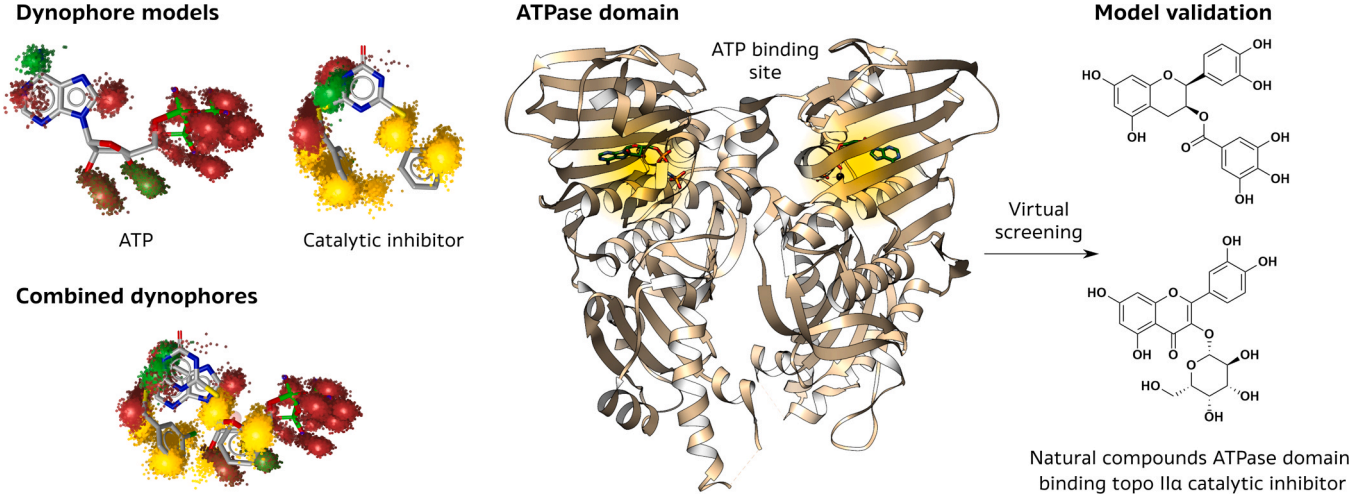

Fig. 1. Overview of the dynophore-based approach for virtual screening using the example of the proof-of-concept validation by identifying flavonoid natural products that act as catalytic topoisomerase IIα inhibitors and bind to the ATPase domain.

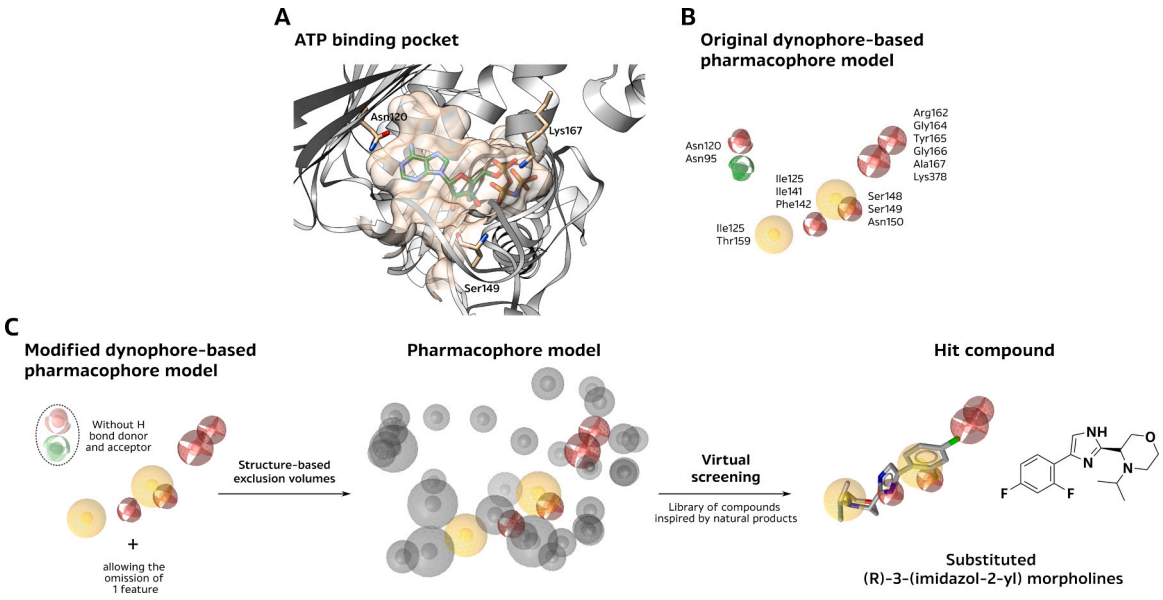

Fig. 2. Dynophore-based molecular design of catalytic topo IIα inhibitors: (A) Visualization of the ATP binding site of human topoisomerase IIα by CASTp. (B) Master dynophore-based pharmacophore from our previous study: hydrophobic features are yellow, hydrogen bond donors are green, and hydrogen bond acceptors are red. (C) Virtual screening cascade: (1) modification of the original master pharmacophore, (2) modified pharmacophore model with exclusion volumes, (3) hit 3-(imidazol-2-yl) morpholine **1** conformation matching this pharmacophore.

lack such cavities, while human topoisomerase IIα, together with some members of the GHKL family, a subfamily of ATPases, has the largest cavity volumes [50].

In many cases, the design of catalytic inhibitors targeting the ATP binding site focuses on interaction with the Asn120 residue, often resulting in compounds containing similar cyclic heterocycles. Such compounds tend to also act as inhibitors of human protein kinases [19, 45]. Here, we wanted to take a different approach and identify the chemical space outside this paradigm and diversify the hits targeting this binding site altogether. Therefore, we decided to investigate in more detail the parts of the binding site where the interaction with the ATPs phosphate and the sugar (ribose) moieties takes place and additionally include one of the empty cavities within the active site, which is located below the adenine moiety. We chose to include this part because our dynophore-based pharmacophore model already contains these features, which were derived from the binding model of 4,6-substituted 1,3,5-triazine-2(1*H*)-ones. The developed dynophore-based pharmacophore model used in our previous study consists of two hydrophobic features, five hydrogen bond acceptors and one hydrogen bond donor. How the pharmacophore features can be attributed to the binding of ATP and triazinone inhibitor is shown in Figs. 1 and 2B. Our modified dynophore-based pharmacophore was designed by omitting the hydrogen bond donor and acceptor features that modeled the interaction with the side chain of the Asn120 residue, thereby no longer explicitly including this structurally positioned interaction in the pharmacophore (Fig. 2C).

The modified dynophore-based pharmacophore model was used in a virtual screening of the NATx library (AnalytiCon Discovery), where the design of the compounds was inspired by natural products or their structural constituents. With these structures, we wanted to search the chemical space containing the unique molecular properties of natural products. In addition, we considered the specific shape of the ATP binding site of topoisomerase IIα by including the exclusion volumes derived from the positions of residues in the ATP binding site as determined by protein crystallography (Fig. 2C). In screening, we allowed the omission of one feature from the full model to identify compounds as hits. From the pool of approximately 32,000 compounds, the screening yielded 186 hits, which were manually reviewed and visualized. We decided to initially focus on hit compounds **1** and **2**, both of which have the 3-(imidazol-2-yl) morpholine core scaffold. Such chemical entities in which imidazole and morpholine moieties are so close to each other, are relatively rare. The design of this class of compounds was inspired by a pharmacophore of the amino acid serine [51], and they also possess favorable drug-like properties.

Based on the pharmacophore model, compound **1** would bind in the ribose and phosphate region of the ATP pocket, while the adenine-binding region would be ignored (Fig. 2C). The phenyl moiety of the compound overlaps the hydrophobic feature that would allow interactions with Ile125, Ile141 and Phe142. The iso-propyl substituent of **1** (and the cyclobuthyl substituent of **2**) is coupled to the hydrophobic feature, which is spatially located in the empty cavity of the ATP binding site. The imidazole moiety of the ligand indicates the possibility of hydrogen bonding with residues Ser148, Ser149 and Asn150. The two fluorine atoms on the phenyl ring are positioned to overlap the hydrogen bond acceptors that mimic the ribose and phosphate interactions with the binding site.

2.2. Hit compounds are catalytic inhibitors of human topo II that bind to the ATPase domain

To validate hit compounds **1** and **2** with the 3-(5-phenyl-1*H*-imidazol-2-yl) morpholine core, we first assessed their inhibitory activity using the topo IIα-mediated relaxation assay with etoposide as a reference. Both compounds inhibited topo IIα-mediated relaxation of DNA in a concentration-dependent manner. The residual activity at a concentration of 50 μM of each compound (RA = 55 % for compound **1** and RA = 81 % for compound **2**) was comparable to etoposide (RA = 81 %) at this concentration (Fig. 3A, S2 and Table S2). To our knowledge, the 3-(1*H*-imidazol-2-yl) morpholine scaffold has not yet been evaluated for topo IIα inhibition. To further evaluate the topo IIα inhibitory activity, we performed a topo IIα-mediated decatenation assay. Again, both hit compounds successfully inhibited the decatenation of kinetoplast DNA (kDNA), an aggregate of interlocking DNA minicircles, in a concentration-dependent manner. At 12.5 μM of compound **1,** only about 15 % of topo IIα activity was detected, while at higher concentrations, the topo IIα inhibition was complete. For compound **2,** approximately 40 % of topo IIα activity was present at 12.5 μM, while all higher concentrations tested produced complete inhibition (Fig. 3B, S3

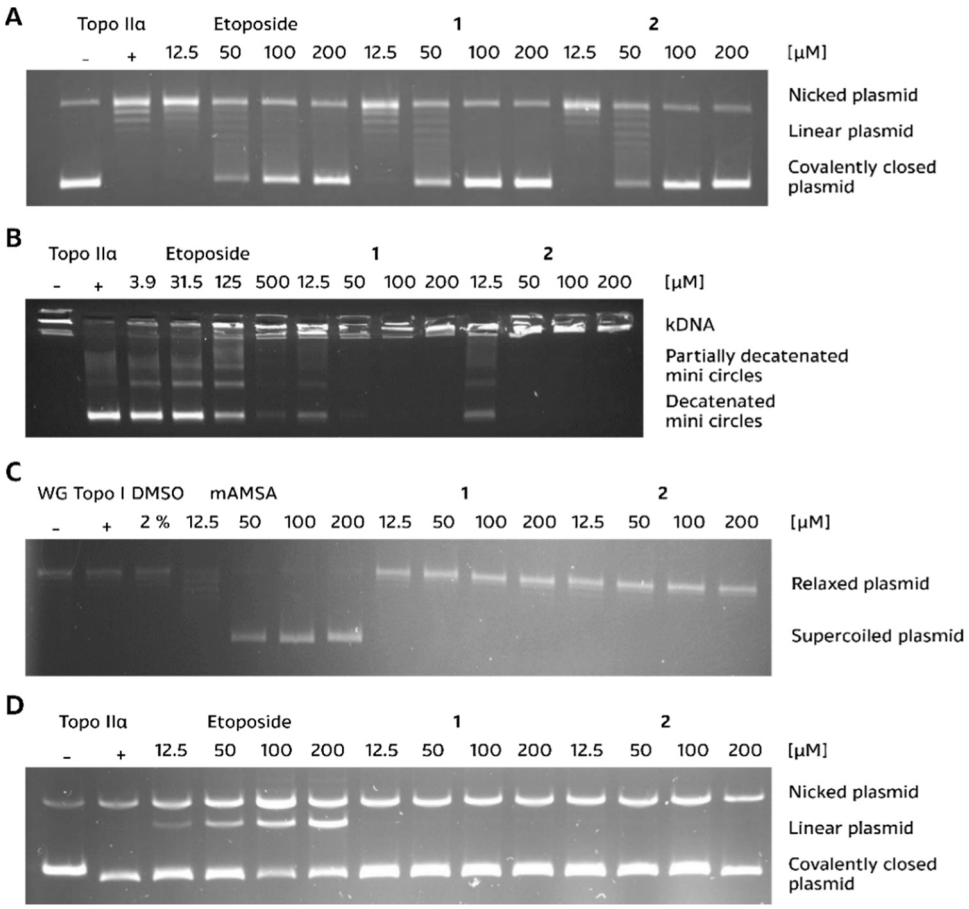

Fig. 3. Biochemical assays of substituted 3-(5-phenyl-1*H*-imidazol-2-yl) morpholine hit compounds: (**A**) Topo IIα-mediated relaxation assay of **1** and **2** and etoposide as positive control. (**B**) Topo IIα-mediated decatenation assay of **1** and **2** and etoposide as positive control. (**C**) Unwinding assay of **1** and **2** and intercalator *m*-AMSA as positive control. (**D**) Topo IIα-mediated cleavage assay of **1** and **2** and etoposide as positive control.

and Table S3).

The inhibition data required a closer examination of the topo IIα inhibition mechanism to determine how well the observed properties fit our molecular design hypothesis. Since topo IIα inhibitors can act as intercalators, we performed the unwinding assay. The effects of intercalation/unwinding of the positive control, the intercalator 4′-(9-acridinylamino) methanesulfone-*m*-anisidine (*m*-AMSA), were observed on the supercoiled substrate at all measured concentrations. Compounds **1** and **2** showed no unwinding activity, indicating that they act as inhibitors rather than intercalators (Fig. 3C, S5). To determine whether these active compounds act as topoisomerase II poisons, a topo IIα-mediated cleavage assay was performed. The etoposide control showed an expected topo II poison activity with a concentration-dependent increase in linear DNA. This effect was not observed for compounds **1** and **2** at any of the concentrations tested, confirming that they do not act as topoisomerase II poisons but as catalytic inhibitors (Fig. 3D, S6, Table S5). This mechanism of action was foreseen in our molecular design. More comprehensive data on the assays performed can be found in Section 4 to 8 of the Supplementary Information.

The experimental results provide enough information to use the computational tools to study the binding interactions. We first performed molecular docking of compound **1**, the more potent of the two substituted 3-(5-phenyl-1*H*-imidazol-2-yl) morpholines in the topo IIα ATP binding site [14]. Compound **1** was modeled as an *R*-enantiomer [51], the configuration in which it was synthesized. Docking calculations revealed two main binding orientations for **1**; one in which the molecule was placed generally in line with the pose identified by the modified dynophore-based pharmacophore model - *Pose 1*, and an alternative pose in which a para fluorine atom on the benzene ring pointed towards the amino acid Asn120 - *Pose 2* (Figure S7) [14].

Since molecular docking only provides a static insight into the protein-ligand complex, we then performed molecular dynamics (MD) simulations with a length of 0.5 μs for both *Poses 1* and *2* to evaluate the molecular recognition from a dynamic and energetic perspective. The conformational stability of the poses varied, as the RMSD for *Pose 1* was 5.2 ± 0.3 Å (Fig. 4A), while it was 6.9 ± 3.0 Å for *Pose 2* (Figure S7, S8). Visualization of the trajectory showed that *Pose 1* underwent an initial adjustment in the first steps of the MD simulation and then stabilized. The structural change is due to the movement of the R_1 2,4-F-phenyl substituent from its initial docking position to a position where it forms interactions with the hydrophobic residue Ile141 (Fig. 4A, B and Figure S8A). In contrast, *Pose 2* first exhibited continuous movement within the ATP binding site and then moved outside of the ATP binding pocket after approximately 300 ns (Figure S8B). Geometric analysis showed that no interaction with Asn120 was observed throughout the simulation, exactly as envisioned in our molecular design.

Given the observed dynamic behavior, we then performed a more comprehensive evaluation of *Pose 1* by first computing dynophore models. While a structure-based pharmacophore only captures a static snapshot of protein-ligand interactions from a docking pose, dynophores can assess the persistence and formation of pharmacophore features over simulation time, providing more reliable insight into the binding modes and interactions that should be prioritized [27]. For *Pose 1*, we observed three sets of interactions: first, a hydrogen bond between the core imidazole and Asn91 and two sets of stable hydrophobic interactions between the R_1 2,4-F-phenyl substituent and the R_2 isopropyl

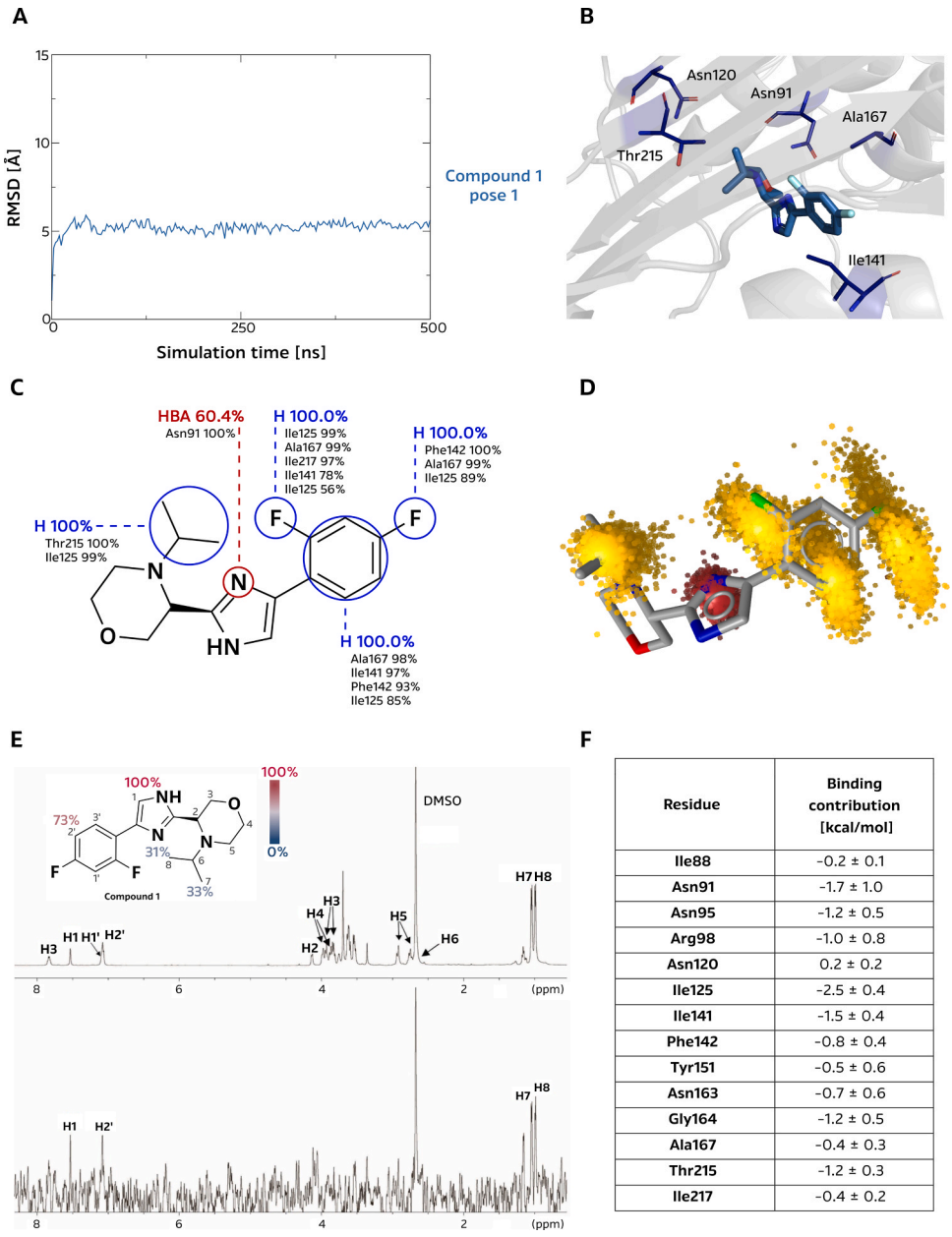

Residue	Binding contribution [kcal/mol]
Ile88	-0.2 ± 0.1
Asn91	-1.7 ± 1.0
Asn95	-1.2 ± 0.5
Arg98	-1.0 ± 0.8
Asn120	0.2 ± 0.2
Ile125	-2.5 ± 0.4
Ile141	-1.5 ± 0.4
Phe142	-0.8 ± 0.4
Tyr151	-0.5 ± 0.6
Asn163	-0.7 ± 0.6
Gly164	-1.2 ± 0.5
Ala167	-0.4 ± 0.3
Thr215	-1.2 ± 0.3
Ile217	-0.4 ± 0.2

Fig. 4. Investigation of the binding of the substituted 3-(5-phenyl-1*H*-imidazol-2-yl)morpholine hit compound **1**: (**A**) RMSD of compound **1** (*Pose 1)* (**B**) MD snapshot of compound **1** (*Pose 1)* in the ATP binding site (**C**) 2D representation of the dynophore of compound **1** and the interaction pattern obtained with the percentages of occurrence of each pharmacophore feature, (**D**) 3D representation of the dynophore of compound **1** (**E**) 1D ^{1}H STD NMR spectra for compound **1** recorded at a protein:ligand ratio of 1:100. The molecular structure illustrates the proton nomenclature and the color-coded relative degrees of saturation of the individual protons. The STD amplification factors were normalized to the intensity of the signal with the largest STD effect. Reference STD spectra (top) with proton assignment and difference STD spectra (bottom) are shown. The STD amplification factors were only calculated for the protons H1, H2', H7, and H8 with sufficient signal-to-noise ratio of the STD signals. The unassigned proton signals between 3.3 and 3.7 ppm belong to the protein buffer containing glycerol. The proton signals were calibrated to the DSS signal at 0.0 ppm. The spectra are not to scale. (**F**) MM/GBSA per-residue decomposition of the binding free energy of compound **1**.

moieties and residues Ile125, Ile141, Phe142, Gly164 and Thr215. During the simulation, the isopropyl moiety of **1** was positioned in the empty cavity below the adenine moiety, as envisioned in the molecular design (Fig. 4C-D). The dynamic geometric aspect of molecular recognition was supported by Molecular Mechanics/Generalized Born Surface Area (MM/GBSA) free energy calculations with a per-residue decomposition (Fig. 4F)[52]. Overall, we found good agreement with the dynophore model results, as a significant contribution from Asn91 is consistent with the observed hydrogen bond, while important energetic contributions from hydrophobic residues such as Ile125, Ile141, Phe142 and Thr215 are consistent with hydrophobic interactions. MM/GBSA calculations also showed that Asn120 does not significantly contribute to ligand binding.

To experimentally evaluate the binding of 3-(5-phenyl-1*H*-imidazol-2-yl)-morpholine compound **1**, we used the isolated human topo-IIα-ATPase domain, in which the targeted ATP binding site is located, and performed Saturation Transfer Difference (STD) NMR experiments (Fig. 4E). In the absence of a crystal structure of the complex between compound **1** and topo IIα, which would provide definitive insight into binding, the STD measurements may provide some relevant structural insights. The experiments confirmed the binding of compound **1** to this domain. The most pronounced STD effect was observed for the proton H1 of the imidazole ring, indicating the involvement of this moiety in the interaction with the protein. The computationally observed

hydrogen bond between the imidazole moiety and Asn91 as well as the energetic importance of this residue support this observation of a favorable interaction. Moreover, a clear STD effect was observed for the protons of the phenyl ring as well as for the protons of the two methyl groups of the isopropyl moiety, suggesting their involvement in the protein-ligand interaction, which is in accordance with our model. The saturation was more intense for the phenyl group, indicating stronger interactions (Fig. 4E). As we later performed STD NMR experiments for other compounds, we point out here that the strength of interactions with the ATPase domain can only be compared between atoms within a given molecule, as the magnitude of the STD enhancement factor also depends on the exchange kinetics of the ligand.

2.3. Structure-activity relationship (SAR) of substituted 3-(imidazol-2-yl) morpholines

After validating the mode of inhibition and binding of compound **1** through a series of experimental and computational assays, we expanded our pool of active substituted 3-(imidazol-2-yl)-morpholines (Table S1). An initial virtual screening of the NATx library identified four compounds from the class of 3-(imidazol-2-yl)morpholines, compounds **1**, **2**, **19**, and one additional untested compound. In total, we now selected a series of 39 additional analogs **3**-**41** and examined them in the topo IIα relaxation assay at a single concentration of 50 μM, which corresponds approximately to the IC_{50} value of etoposide (Figure S9, S10, Table S6, Table S7). Compounds were selected to cover diverse available chemical space using a 3-(imidazol-2-yl)morpholines substructure search of the NATx library. It was encouraging to observe that many compounds showed inhibition of topo IIα, resulting in less than 50 % residual activity. For the most promising 26 compounds, we performed this assay at 4 concentrations and determined the IC_{50} values (Tables 1 and 2, Figure S11, S12, Tables S8, S9). Among the active compounds, many have an IC_{50} value of topo IIα inhibition of less than 10 μM. In addition, the members of the 3-(imidazol-2-yl)morpholines exhibit favorable solubility and their moderate molecular weight allows further optimization and development of compounds.

Based on the inhibition data, we were able to outline the first structure-activity relationship (SAR) of the 3-(imidazol-2-yl)morpholine series. Compounds **1**-**32** of the first series all contain a substituted phenyl group at the R_1 position with respect to the imidazole core (Table 1). Favorable effects on IC_{50} values were observed for compounds containing mono-fluorophenyls such as 4-CF_3 (compounds **9** and **10**), 4-OCF_3 (compound **13**), 4-F (compound **17**, **18**), 3-F (compounds **23**, **24**, **26**). The mono-chlorophenyl substituents, in particular 4-Cl and 3-Cl (compounds **5**, **27**, **28**, **30** and **32**), also exhibited IC_{50} values in the range of 10 μM and below. As for the substituents at the R_2 position, isopropyl, cyclobuthyl and cyclopropylmethyl were favorable. Significant lengthening of R_2 by introducing a substituted phenyl also enabled strong topo IIα inhibition (compound **17**). On the other hand, 3-(imidazol-2-yl) morpholine **3**, in which R_2 was unsubstituted, displayed lower inhibitory activity. It seems that R_2 substitution is mandatory to achieve potent topo-IIα inhibition. The introduction of 1*H*-imidazol-4-yl, piperidin-4-yl or N,N-dimethylaniline at the R_2 position (compounds **6**, **11**, **20**, **25**, **31**), was also not favorable. Looking at the active compounds, the introduction of a fluoro or chloro substituent seems to be favorable (Table 1).

To investigate the effects of the lengthening of R_2 on the bound conformation of substituted 3-(imidazol-2-yl)morpholines, we performed molecular docking of compound **17**. We observed a stacked conformation in which the R_1 4-fluorophenyl resembled the corresponding R_1 2,4-F-phenyl in *Pose 1* of compound **1**, while the R_2 4-Cl-phenyl adopted a conformation akin to the MD-equilibrated position of R_1 in compound **1** and interacted with residues such as Ile141 (Animation 1, Figure S8, S18). Remarkably, no docking solutions were found that positioned the R_2 substituent of **17** towards the vacant cavity below the adenine moiety, as was observed with shorter substituents. This suggests that this cavity remains inaccessible for compounds with two aromatic substituents, as stacking seems to be favorable over an extended conformation.

In the second series, comprising compounds **33**-**41**, the R_1-phenyl substituent was replaced by either 5-chlorothiophene-2-yl, pyridine-3-ly or pyridine-4-yl (Table 2). This modification generally resulted in topo IIα inhibition with IC_{50} values below 10 μM. Compounds **34** and **40**, which are direct analogs of compound **1**, and compounds **37** and **39**, analogs of compound **2**, all showed improved inhibition compared to the corresponding R_1-phenyl-substituted compounds. In addition, the presence of R_2 1*H*-imidazol-4-yl, piperidin-4-yl substituents (compounds **36** and **41**) resulted in a weaker inhibitory effect, which is in good agreement with observed SAR of the first series. Overall, the investigation of the available compounds provided initial insights into the SAR of substituted 3-(imidazol-2-yl)morpholines, which can form the basis for subsequent ligand optimization through the synthesis of novel analogs.

We further investigated the effects of R_1 modifications in the second series by molecular docking. The placement of the R_1 5-chlorothiophene moiety in compounds **33** and **34** was consistent with that observed for R_1-substituted phenyls in the previous series. In addition, two different positions of the R_2 substituent in respect to its length were observed in this pair of compounds. The shorter isopropyl R_2 substituent was aligned with the vacant cavity in the ATP pocket, while the longer 4 F-phenyl was positioned to interact with Ile141, similar to the stacked pose of compound **17**. In agreement with these observations, docking of compound **38** with R_1 pyridine-3-yl substituent aligned with the aforementioned findings, where R_1 cyclopropyl was expectedly placed towards the empty cavity (Figure S18). Overall docking results suggest that 5-chlorothiophene and pyridine interact with the same region of the ATP binding site, forming stronger interactions than substituted phenyls.

Additionally, we evaluated the inhibition of the topo IIβ isoform for hit compounds **1** and **2** and active compounds **17**, **33**, **34, 35** and **38** we identified in SAR investigations using the topo IIβ-mediated relaxation assay. Both hit compounds were able to inhibit topo IIβ, with barely any selectivity between the two enzyme isoforms. Furthermore, the topoisomerase IIβ-mediated relaxation assay, of **17**, **33**, **34, 35** and **38** yielded IC_{50} values of 19.2, 3.03, 2.68, 3.14 and 3.38 μM respectively (Figure S4 and Table S4). These values are fully comparable with inhibitory effect observed on the topo IIα isoform showing that compounds can effectively inhibit both α and β isoforms. Previous studies have made limited attempts to distinguish catalytic inhibitors between the two topo II isoforms. However, recently reported tetrahydroquinazoline inhibitors, which do not act as topo II poisons, show that selective inhibition of topo IIα over the topo IIβ isoform is possible. [53–56]. However, it is worth noting that for topo II poisons, selectivity towards over topo IIα is favored due to the DNA damage associated with their use [57]. However, since the isoform IIβ could compensate for the absence of topo IIα in certain cell lines [10,11], concurrent inhibition of both isoforms could be beneficial, especially for catalytic inhibitors.

The initial virtual screening of the NATx library using our modified dynophore-based pharmacophore yielded 186 hits; four of which were 3-(imidazol-2-yl)morpholines, three of which were tested. This result is not surprising as our screening pharmacophore was primarily designed to “fish out” hit compounds of new chemical classes with desired properties. The docking results indicate that the molecular recognition of this chemical class to be complex, with both stacked and extended conformations depending on the substituents. Subsequent investigation of this pharmacophore revealed that only compounds containing the 2,4-diflurobenzyl moiety at the R_1 position could fulfill the constraints of the pharmacophore. When we relaxed the conditions and rendered an additional hydrogen bond acceptor as optional and repeated the screening, we identified 26 of the 42 compounds tested, as opposed to only four.

Table 1
Results of the topoisomerase IIα relaxation assay of the first series of substituted 3-(imidazol-2-yl) morpholine compounds.

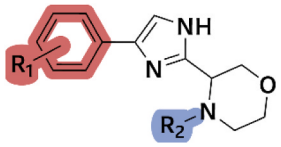

N	R_1	R_2	IC_{50} [μM]	N	R_1	R_2	IC_{50} [μM]	N	R_1	R_2	IC_{50} [μM]
1	2,4-F		45,0	**12**	4-CF_3	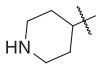	> 50	**23**	3-F		10,7
2	2,4-F		> 50	**13**	4-OCF_3		5,2	**24**	3-F		5,6
3	4-Cl	H	> 50	**14**	4-F		44,6	**25**	3-F	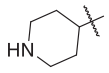	> 50
4	4-Cl		> 50	**15**	4-F		44,0	**26**	3-F		9,3
5	4-Cl		16,7	**16**	4-F	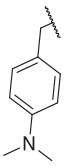	43,1	**27**	3-Cl		2,1
6	4-Cl	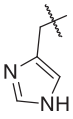	> 50	**17**	4-F	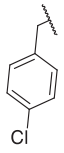	9,4	**28**	3-Cl		4,6
7	4-Cl	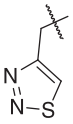	19,3	**18**	4-F		7,4	**29**	3-Cl	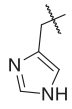	> 50
8	4-Cl		43,7	**19**	2,4-F		10,3	**30**	3-Cl	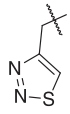	4,6
9	4-CF_3		29,6	**20**	2,4-F	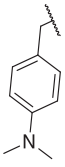	> 50	**31**	3-Cl	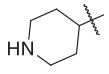	> 50
10	4-CF_3		9,4	**21**	2,4-F	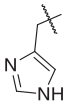	> 50	**32**	3-Cl		1,4
11	4-CF_3	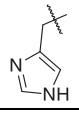	> 50	**22**	2,4-F	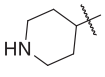	> 50				

Measurements are the average of two independent experiments.

Table 2
Results of topoisomerase IIα relaxation assay of the second series of substituted 3-(imidazol-2-yl)-morpholine compounds.

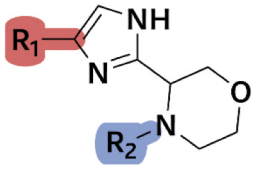

N	R_1	R_2	IC_{50} [μM]	N	R_1	R_2	IC_{50} [μM]
33	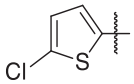	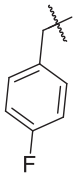	2,5	**38**	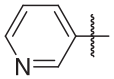		2,1
34	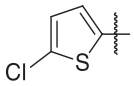		4,4	**39**	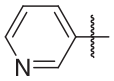		2,9
35	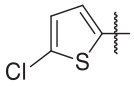		1,4	**40**	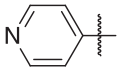		2,4
36	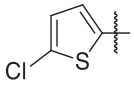	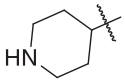	> 50	**41**	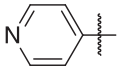	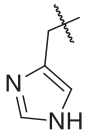	> 50
37	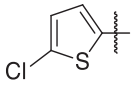		1,0				

Measurements are the average of two independent experiments.

2.4. Substituted 3-(imidazol-2-yl) morpholines are cytotoxic against human cancer cells via a mechanism distinct from topoisomerase II poisons

2.4.1. Cytotoxicity of 3-(imidazol-2-yl) morpholines

Based on the encouraging *in vitro* data, we investigated the cytotoxicity of 18 selected active 3-(imidazol-2-yl) morpholines on the human hepatocellular (HepG2) and human breast cancer (MCF-7) cell lines using the MTS assay Table S15. The two selected human cancer cell lines are representative of a standard cell-based system for *in vitro* assessment of the anticancer potential of compounds, which was also used in our previous studies [24,58,59]. An initial screening was performed on exponentially growing cells exposed to one concentration of the selected compounds for 24 and 72 hours, using etoposide as a positive control (PC).

Seven compounds were identified that significantly reduced the viability of the tested cell lines. In particular, for the HepG2 cell line compounds **10, 13, 17, 28, 33, 34**, and **35** reduced cell viability by more than 40 % after 24 hours of exposure, and compounds **10, 13, 17, 28, 33**, and **34** reduced cell viability by more than 50 % after 72 hours of exposure. For the MCF-7 cell line, only compounds **10, 17, 33**, and **32** and compounds **10**, **17**, and **33** reduced cell viability by more than 40 % and 50 % after 24- and 72-hours treatment, respectively (Fig. 5A-B).

On the basis of this screening, we selected compounds **10, 13, 17, 28, 33, 34,** and **35** for further concentration-dependent experiments and determination of the EC_{50}. The cytotoxicity of the selected compounds and of etoposide as a positive control was determined in at least three concentrations after 24- and 72-hour treatments. Overall, the results showed the most promising effect of compound **17**, which had the lowest EC_{50} value observed in both cell lines tested, namely 47.5 μM in HepG2 cells and 86.8 μM in MCF-7 cells after 72-hour exposure. Compound **33** was the second most potent compound with EC_{50} values of 82.7 μM in HepG2 and 85.6 μM in MCF-7 cells after 72 hours of treatment. The determined dose-response curves for compounds **17** and **33** are presented in Fig. 5C and D. The EC_{50} values determined for etoposide at 72-hour exposure were in the same concentration range as the compounds tested and were comparable with previously published data (Figure S20 Table S15) [58,60].

Three substituted 3-(imidazol-2-yl) morpholines**,** the first hit **1** and the most promising compounds, **17** and **33**, were sent to the National Cancer Institute (USA) where they were approved for NCI-60 screening. This assay is performed on a panel of 60 different human cancer cell lines, ranging from leukemia, lung, colon and central nervous system cancer, melanoma, ovarian, kidney, prostate and breast cancer. NCI-60 screening of compound **1** showed no significant cytotoxic activity, consistent with the very low MTS cytotoxicity observed with the HepG-2 and MCF-7 cell lines (Fig. 6). In contrast, compounds **17** and **33** exhibited stronger cytotoxicity (Fig. 6, S21). The average growth percentage of all cancer cell lines was unfortunately not high enough to consider the compounds for the NCI-60 concentration-dependent experiments, but screening at one concentration already revealed several human cancer cell lines in which growth was significantly impaired. The relevant human cancer cell lines were leukemia cancer (chronic myeloid leukemia (K-562), T-cell leukemia (MOLT-4), multiple myeloma (RPMI-8226), lymphoma (SR)), melanoma cancer (malignant melanoma

(MALME-3 M, SK-MEL-5) and melanotic melanoma (UACC-62)), ovarian cancer (NCI/ADR-RES) and breast cancer (breast adenocarcinoma (MCF-7, MDA-MB-468), breast carcinoma (HS 578 T)). The MCF-7 cell line results align well with our cytotoxicity results for compounds **1**, **17** and **33**, providing further validation (Fig. 6 and S21, S22).

Cancer cytotoxicity data suggest that some of the substituted 3-(imidazol-2-yl)morpholines studied have significant potential for initiating optimization efforts as well as more advanced preclinical research, particularly focused on leukemia, melanoma, ovarian and breast cancer. According to the Human Protein Atlas (Figure S23 A-C)[61] and the Human Proteome Map (Figure S23 D) [62], the enzyme topoisomerase IIα is predominantly expressed in skin, bone marrow, lymphoid tissues (e.g. bone marrow, appendix, thymus, spleen), lymph nodes and tonsils, as well as in male and female specific tissues. The sensitivity observed in the NCI-60 screening and in our cytotoxicity experiments is therefore a promising starting point for the further anticancer development of this compound class against these types of cancers.

2.4.2. Effects of 3-(imidazol-2-yl) morpholines on cell cycle, cell proliferation, and induction of DNA double-stranded breaks

Since compound **17** was identified as the most potent compound in the cytotoxicity assays, we wanted to further investigate the potential effects of the selected compound on cell proliferation. The effects on proliferation and cell cycle distribution of HepG2 and MCF-7 cells were examined after 24 and 72 hours of exposure (Fig. 7 and S24). The reduction in cell proliferation was confirmed by a decrease in the number of Ki67-positive HepG2 and MCF-7 cells at the highest concentration tested after 24- and 72-hour exposure. The highest concentration of compound **17** tested was 50 μM for the 24-hour 72-hour treatment, which already caused a 40 % decrease in cell viability in both

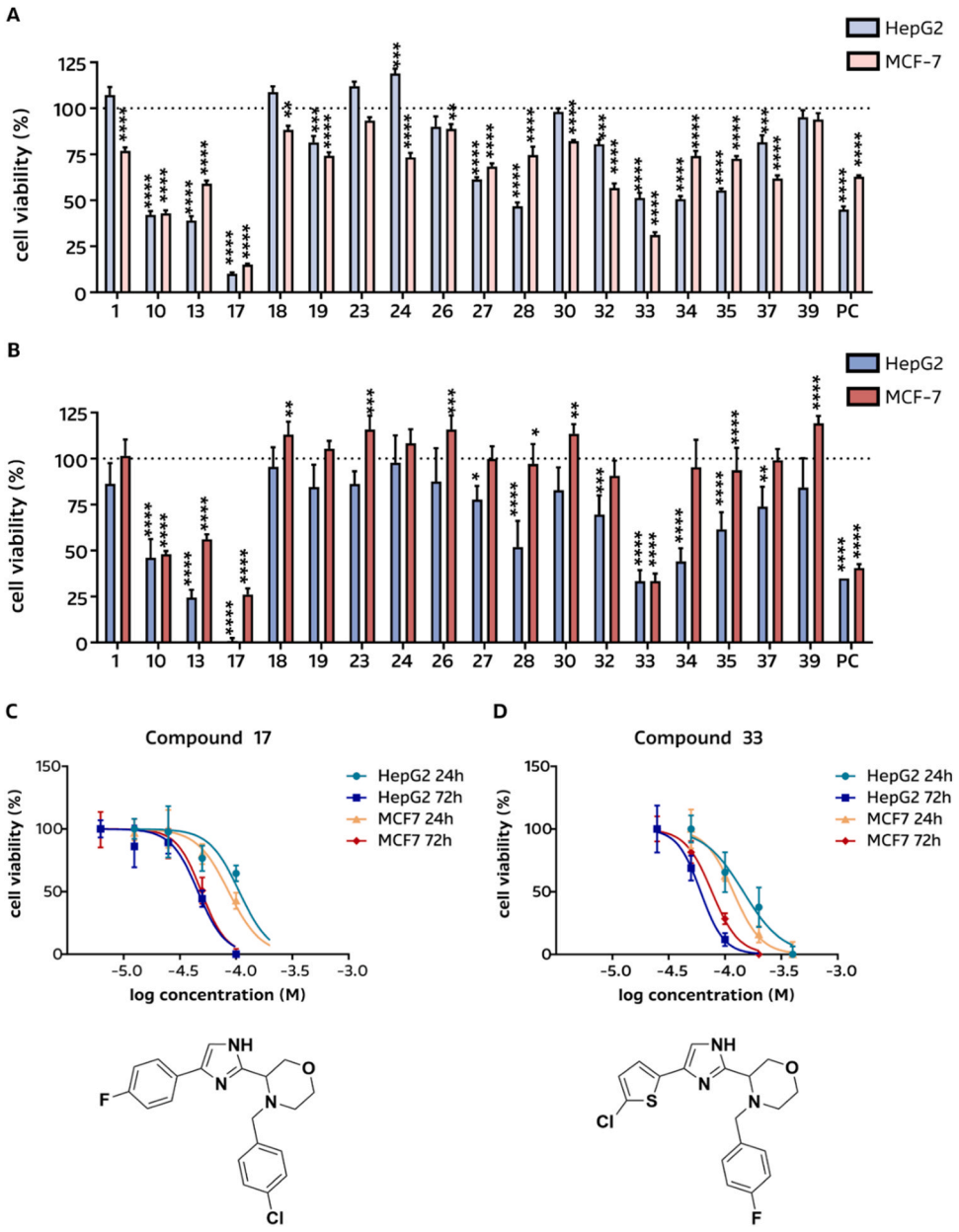

Fig. 5. Results of preliminary cytotoxicity screening using the MTS assay for selected active compounds. HepG2 and MCF-7 cells were exposed to the investigated compounds and the positive control (PC, etoposide) at concentrations of (**A**) 200 μM for 24 h and (**B**) 100 μM for 72 h. Significant differences between solvent control (DMSO 0.2 %) and treated cells were calculated using ANOVA and is indicated * (*$p < 0.05$, **$p < 0.01$, ***$p < 0.001$, ****$p < 0.0001$). **(C-D)** Dose−response curves for the most potent compounds **17** and **33** of HepG2 and MCF-7 cells after treatment (24 or 72 hours). Experiments were performed in five replicates and repeated three times independently, and the standard deviation (SD) was calculated.

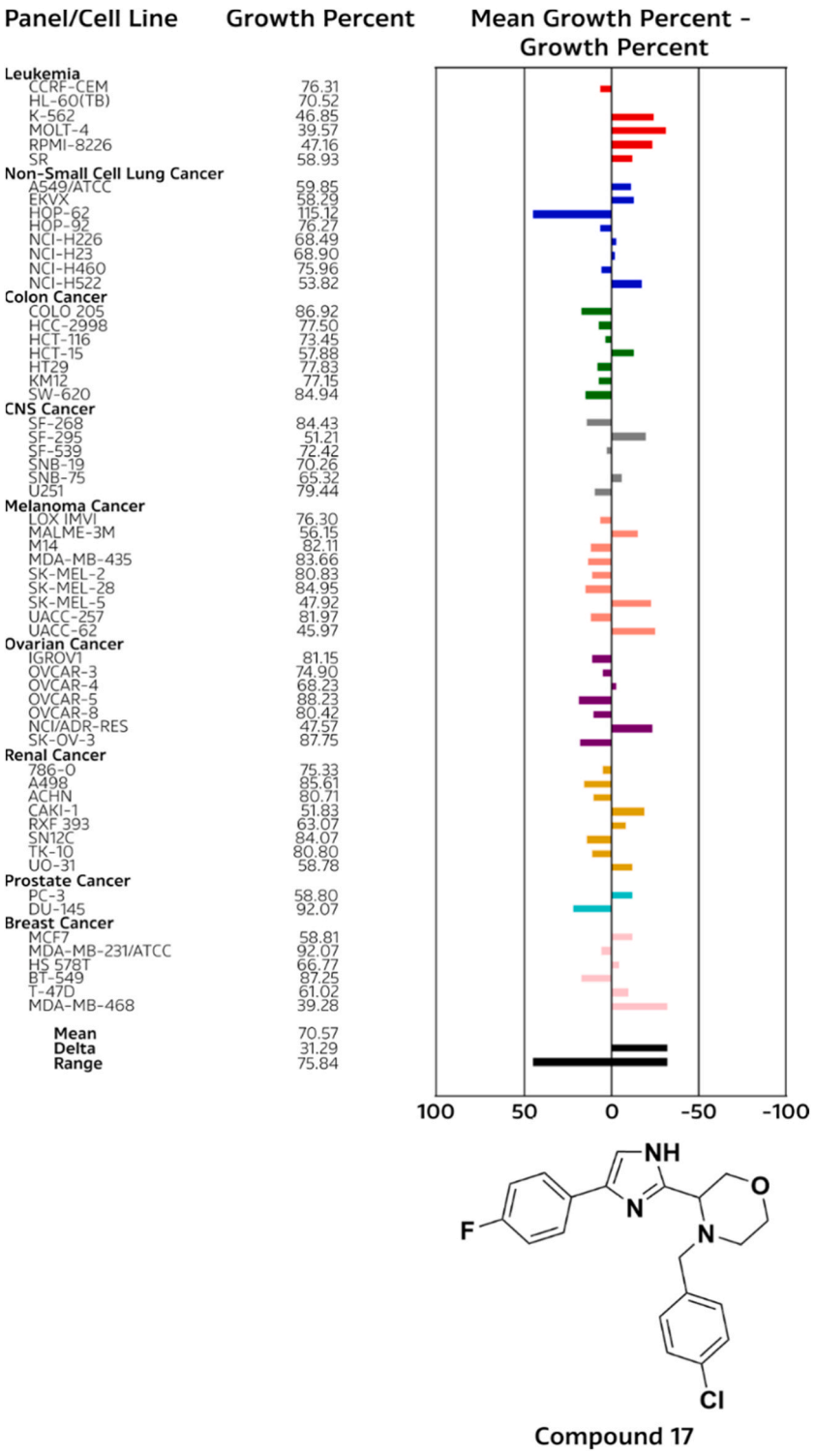

Fig. 6. Results of the NCI-60 screening of 3-(imidazol-2-yl)-morpholine hit compound **17**.

cell lines tested.

Consistent with the observed decrease in Ki67 marker expressed in all cell phases except G0 phase of quiescent cells, we observed a significant change in cell cycle distribution in HepG2 cells after 24 hours of treatment and in MCF-7 cells after 72 hours of treatment with the highest concentrations tested. The results showed that cells accumulated in the G0/G1 phase, indicating cell arrest in the G0 phase. In contrast, the positive control etoposide, a topoisomerase II inhibiting anticancer drug [63], significantly reduced cell proliferation and caused cell accumulation in the G2/M phase of the cell cycle in HepG2 and MCF-7 cells at both exposure time points. Thus, these results suggest that the investigated compound **17** acts via a different cellular pathway than clinical topoisomerase II poisons (Fig. 7B, E and S23).

The latter was confirmed by analyzing DNA double-strand breaks (DSBs), which were determined by detecting γH2AX foci in each individual cell by measuring the fluorescence signals using flow cytometry. DNA double-strand breaks (DSBs) are a common side effect of chemotherapy with topoisomerase II poisons, including etoposide, as

previously mentioned [64]. Exposure of HepG2 and MCF-7 cells to compound **17** did not result in the formation of γH2AX after 72 h of exposure (Fig. 7C, F and S23).

2.5. Substituted 3-(imidazol-2-yl) morpholines: inhibition, selectivity, and binding properties

The assays conducted on human cancer cell lines identified the most promising representatives of 3-(imidazol-2-yl)-morpholines, with compounds **17** and **33** standing out. To confirm their mechanism of action, we initiated a detailed investigation analogous to hit compound **1**.

The topoisomerase IIα-mediated relaxation assay already provided information on the concentration range in which the compounds fully inhibit topo IIα, thus we decided to use lower concentrations in the topoisomerase IIα mediated decatenation assay (Fig S13, Table S10). Complete inhibition of decatenation of kDNA was found at the 12.5 and 50 μM concentrations of both compounds, and only moderate enzyme activity was observed at the 0.781 and 3.125 μM concentrations of compound **17** and 0.781 μM for compound **33**.

Furthermore, no intercalation effect was observed for either compound (Fig S14), and the cleavage assays showed no increase in linear plasmid with increased compound concentration, confirming that the compounds act as catalytic inhibitors (Fig S15, Table S11). For these compounds, we also performed a competitive cleavage assay with the constant 50 μM concentration of etoposide and in both cases, we observed a decrease in linear plasmid at increased concentrations of compounds **17** and **33**, the latter being more effective (Fig S16, Table S12). The full data for the assays performed with these promising hit compounds can be found in Supplementary information Section 12-14.

Since our molecular design was coupled with structural specificities of the ATP binding site of topo IIα, we were naturally interested in verifying whether inhibition specificity could be observed for this class of compounds, especially in comparison to human protein kinases. Therefore, we tested the first 3-(imidazol-2-yl)morpholine hit compound **1** as well as the hit compound **17** on a group of 20 human protein kinases. From this set of 20 human protein kinases, 9 members – CDK1/CyclinB, IGF-1R, JAK2, Flt-3, Src, PKA, PKB, Ret and FGFR3 were selected based on the evaluation of a preclinical 9*H*-purine-based candidate that functioned as an ATP-competitive catalytic inhibitor of topo IIα [11]. The additional 11 human kinases were selected from members used in studies of simultaneous inhibition of topoisomerase IIα and human protein kinase(s), primarily to evaluate a potentially beneficial dual effect to improve cancer therapy [65]. Apart from a slight inhibition of some kinases, no significant inhibitory effect was observed for either compound **1** or compound **17** at the 10 μM concentration used

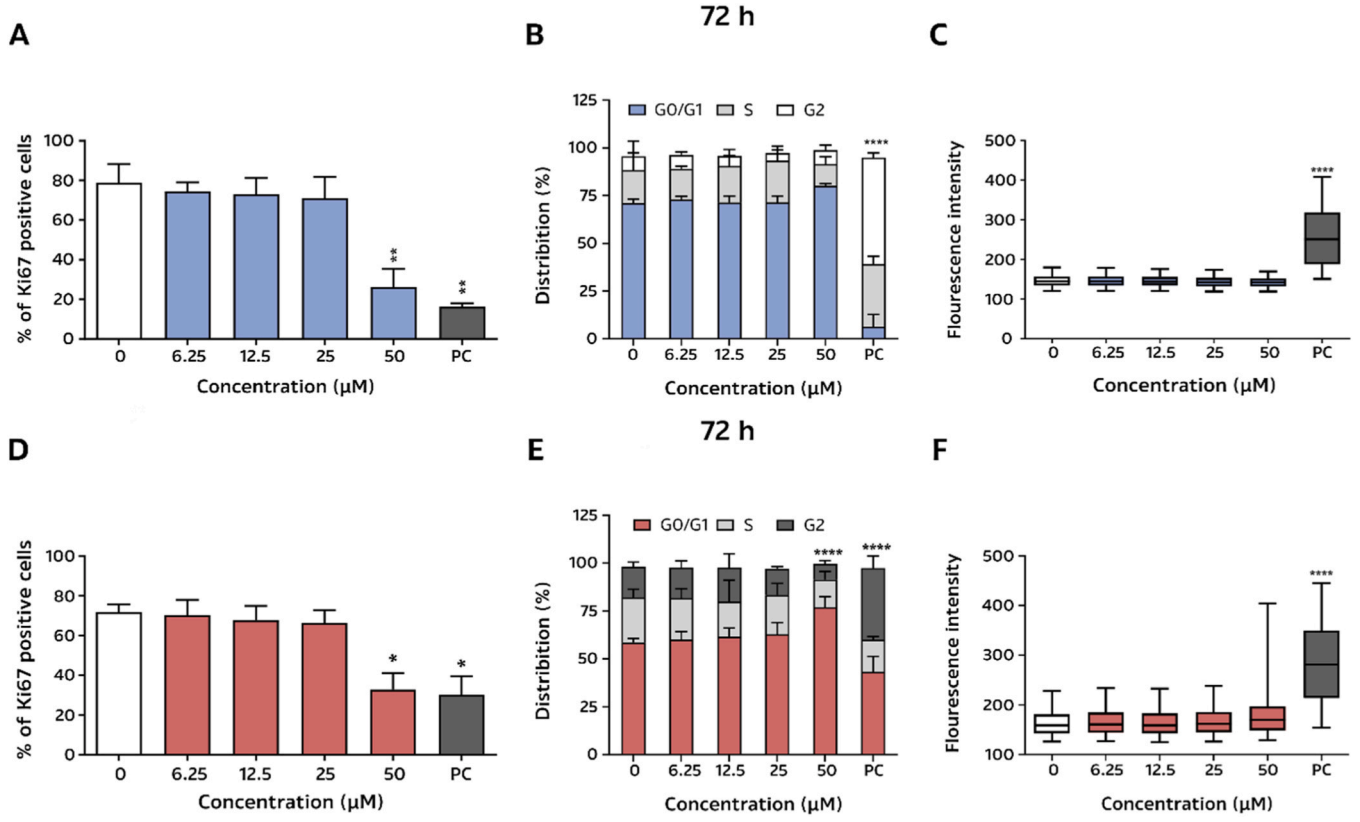

Fig. 7. (*Above*) Flow cytometric analysis of Ki67 expression, cell cycle distribution, and induction of the DNA double-stand breaks (DSBs) in HepG2 cells after 72-hour exposure to compound **17** (**A**) Percentage of Ki67-positive cells in HepG2 cells after 72-hour exposure to compound **17**. (**B**) Distribution of HepG2 cells in the phases of cell cycle after 72-hour treatment. (**C**) Quantile box plots (95 % confidence interval) represent the relative values of fluorescence intensity corresponding to sites labelled with anti-γH2AX to detect DNA double-strand breaks in HepG2 cells after 72-hour exposure to the selected compound **17**. Etoposide was used as a positive control (PC) and was included in each parallel. Three independent experiments were performed. Significant difference between solvent control cells (0) DMSO and cells exposed to compound 17 and PC is indicated * (*$p < 0.05$, **$p < 0.01$, ****$p < 0.0001$). (*Bellow*) Flow cytometric analysis of Ki67 expression, cell cycle distribution, and induction of the DNA double-stand breaks (DSBs) in MCF-7 cells after 72-hour exposure to the compound **17**. (**D**) Percentage of Ki67-positive cells in MCF-7 cells after 72-hour exposure to compound **17**. (**E**) Distribution of MCF-7 cells in the phases of cell cycle after 72-hour treatment. (**F**) Quantile box plots (95 % confidence interval) represent the relative values of fluorescence intensity corresponding to sites labelled with anti-γH2AX to detect DNA double-strand breaks in MCF-7 cells after 72-hour exposure to the selected compound. Etoposide was used as a positive control (PC) and was included in each parallel. Three independent experiments were performed. A significant difference between the solvent control cells (0) and the cells exposed to compound **17** and PC is indicated by * (*$p < 0.05$, ****$p < 0.0001$).

(Table 3). These results indicate that substituted 3-(imidazol-2-yl)morpholines can selectively inhibit topoisomerase IIα compared to several relevant human protein kinases.

In order to analyze the binding model of the most promising hit compounds, to compare it with the molecular recognition of the hit compound **1** and to provide guidelines for the future optimization of substituted 3-(imidazol-2-yl)-morpholines, we again performed computational studies. Hit compound **17** was selected here as it showed slightly better cytotoxic properties compared to **33**. This compound was also evaluated by flow cytometry experiments and showed overall the most comprehensive characterization of all compounds. A docked pose of compound **17** (its *R*-enatiomer) in the ATP binding pocket was simulated in a 0.5 μs long MD and was found to be very stable (RMSD = 1.3 ± 0.3 Å) (Fig. 8A, B and S19A). Dynophore analysis also revealed a stable and less scattered pattern of pharmacophore features compared to hit compound **1**. Such a stable interaction pattern is in line with the improved IC_{50} of **17** over **1** (Fig. 8C, D and S19B). The pharmacophore features can be grouped into three interaction patterns: hydrogen bonds between the imidazol-2-yl morpholine core and Ser149, followed by two clusters of stable hydrophobic interactions. The first occurs between R_1 4 F-phenyl and hydrophobic residues such as Ile88, Val90, Ala167 and reflects a new position of the R_1 residue in the binding site compared to compound **1**. The R_2 4Cl-phenyl moiety forms hydrophobic interactions predominantly with residues Ile141 and Phe142 (Fig. 8D and Figure S19B). This positioning of the R_1 and R_2 substituents together with the larger size of R_2 appears to allow a more efficient interaction pattern compared to compound **1.** The MM/GBSA analysis was consistent with the dynophore and showed favorable interactions with all the mentioned residues, highlighting in particular the importance of Ile141 and Val 90. The H-bond interaction with Ser149 was also among the more important contributions, and again no energetic effects of Asn120 were observed (Fig. 8F).

To further substantiate the binding model, we selected the promising hit compounds **17** and **33** and again performed the STD NMR binding study on the human topo IIα ATPase domain (Fig. 8E and S17). The experiments confirmed the binding of the two compounds to the topo IIα ATPase domain. The strongest STD effect observed for the proton H1 of the imidazole ring can be related to the computationally observed hydrogen bonding between the imidazole moiety of **17** and Ser149, and its energetic significance is also present in the MM/GBSA calculations. Furthermore, the replacement of the isopropyl group by a para-substituted benzyl ring at the R_2 position in both measured compounds unifies the STD effects of the R_1 and R_2 substituents. This suggests a stronger interaction of these compounds with the ATP binding pocket compared to compound **1**. These conclusions are consistent with the dynamics and energetics of the computational model for the binding of compound **17** at the target binding site.

Table 3
Inhibitory properties of compounds **1** and **17** tested on a panel of 20 human protein kinases.

Human protein kinase	Compound. 1 [% activity]	Compound 17 [% activity]
B-Raf	78	79
CDK1/cyclinB	92	95
cKit	126	103
c-RAF	91	95
EGFR	93	96
FGFR1	82	111
FGFR3	81	98
Flt1	103	96
Flt3	96	98
Fms	98	102
IGF-1R	108	113
JAK2	110	117
MEKK3	96	99
PDGFRα	97	101
PKA	112	114
PKBα	111	110
Ret	93	103
Src	99	73
ATM	108	118
DNA-PK	90	72

3. Conclusion

Human DNA topoisomerase IIα is a fundamental player in the process of cellular replication and inhibitors of topoisomerase IIα hold immense potential for cancer chemotherapy. The current clinical topoisomerase II poisons cause side effects such as secondary tumors that are directly related to their mechanism of action, which causes DNA damage, therefore the development of inhibitors with novel mechanisms of action is crucial and catalytic inhibitors are among the promising future paradigms. The initial dynophore-based pharmacophore model validated by flavonoid-based topo IIα inhibitors was here modified and successfully applied to the molecular design of a new class of catalytic inhibitors targeting the ATP-binding site of DNA topoisomerase IIα. In virtual screening, instead of conventional synthetic libraries of small molecules, we used nature-inspired libraries of compounds derived from natural products, that combine nature's inventiveness with a chemist's rationality. We have identified the substituted 3-(imidazol-2-yl)morpholine hits **1** and **2** and performed extensive mechanistic studies to confirm their catalytic inhibition mechanism and binding to the ATPase domain. Our derived computational binding model and the experimental binding results are consistent with the screening pharmacophore. Structure-activity relationship (SAR) exploration for this chemical class revealed compounds that exhibit inhibitory IC_{50} values in the single-digit micromolar range. Cancer cytotoxicity measurements and the NCI-60 screening have shown that the compounds have the potential to kill leukemia, melanotic melanoma, ovarian and breast cancer human cell lines, cancers for which topoisomerase II-targeted drugs are commonly used. In addition to confirmed catalytic inhibition and binding to the ATPase domain, the research flagship compound **17**, also exhibits selectivity towards human protein kinases and has a cytotoxicity mechanism where no DNA damage occurs as a side-effect and is distinct from the effect of clinical topoisomerase II poisons. Furthermore, compound **17** proved to be selective for topo IIα when tested against a range of human protein kinases and with its favorable solubility and molecular weight, enables further optimization. In summary, this study demonstrates the innovative chemistry of the nature-inspired substituted 3-(imidazol-2-yl)morpholines and the successful implementation of a molecular design strategy that incorporates a dynamic component of target-ligand molecular recognition with comprehensive experimental characterization, leading to validated hit compounds with potential impact on the development of safe chemotherapies.

4. Experimental section

4.1. Dynophore-based pharmacophore model and virtual screening

The dynophore-based pharmacophore model used in the virtual screening campaign was created as described in Section 2.1. It utilized the pharmacophore data derived from the validation of the dynophore-based approach in molecular design, with the ATP binding site of topo IIα serving as the model target. The source for screening molecules was the NATx compound library from AnalytiCon Discovery, whose design was primarily inspired by biologically relevant full or partial structures of natural products [66], with the number of compounds in this library being approximately 32,000. The 3D conformational models of the molecules were created with the iCon conformer generator in LigandScout using the best settings, resulting in approximately 25 conformations per compound. Virtual screening was then performed in LigandScout using the default settings. The hits that matched the

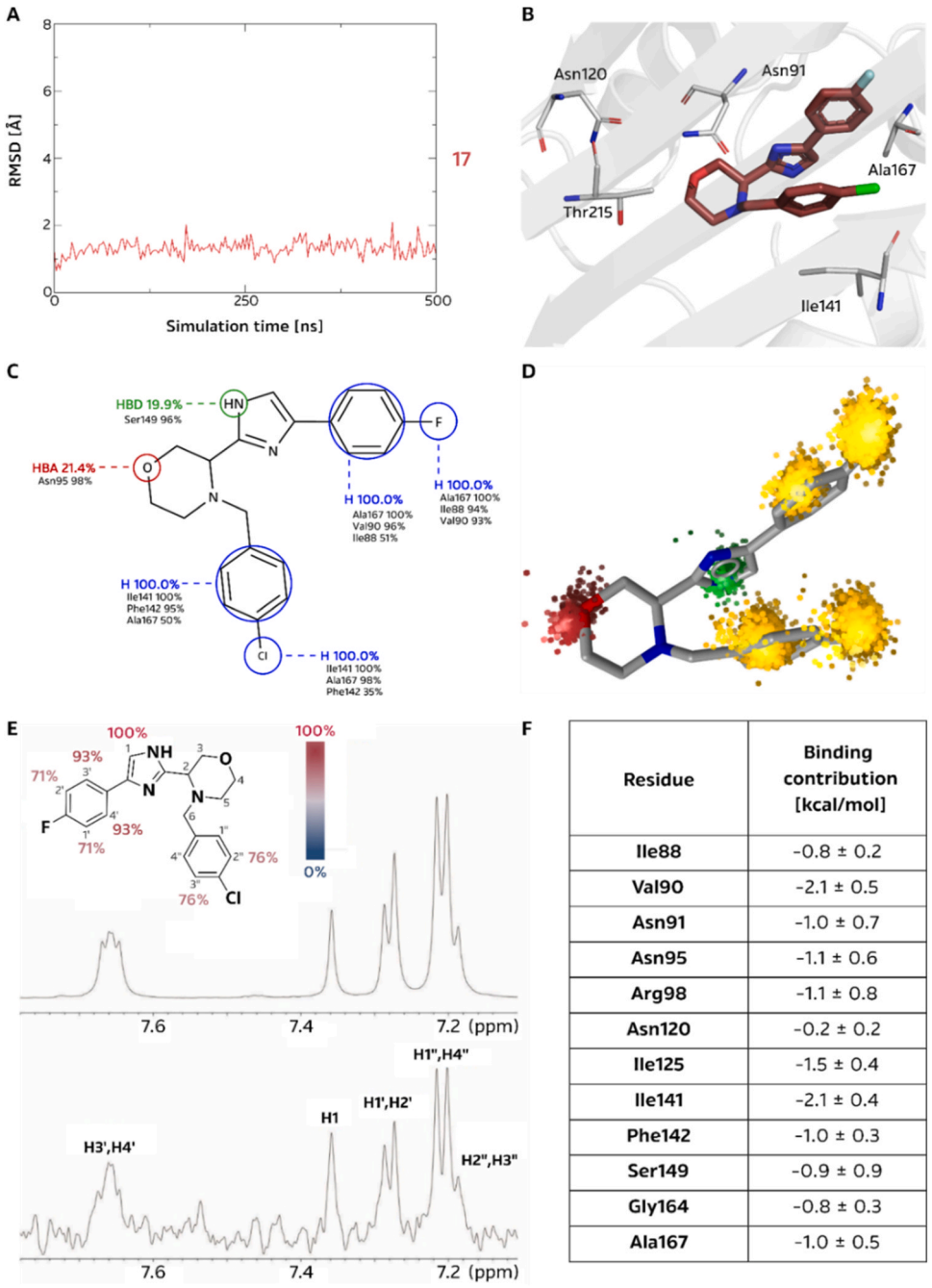

Residue	Binding contribution [kcal/mol]
Ile88	-0.8 ± 0.2
Val90	-2.1 ± 0.5
Asn91	-1.0 ± 0.7
Asn95	-1.1 ± 0.6
Arg98	-1.1 ± 0.8
Asn120	-0.2 ± 0.2
Ile125	-1.5 ± 0.4
Ile141	-2.1 ± 0.4
Phe142	-1.0 ± 0.3
Ser149	-0.9 ± 0.9
Gly164	-0.8 ± 0.3
Ala167	-1.0 ± 0.5

Fig. 8. Hit compound **17** binding study: (**A**) RMSD of compound **17** (**B**) MD snapshot of compound **17** in the ATP binding site (**C**) 2D representation of the dynophore of compound **17** and the interaction pattern obtained with percentage occurrence of each pharmacophore feature, (**D**) 3D representation of a dynophore of compound **17** (**E**) The aromatic part of the 1D ^{1}H STD NMR spectra for compound **17** at a protein:ligand ratio of 1:100. The molecular structure illustrates the proton nomenclature and the color-coded relative degrees of saturation of the individual protons. The STD amplification factors were normalized to the intensity of the signal with the largest STD effect. Shown are reference STD spectra (top) and difference STD spectra (bottom) with proton assignment. Only aromatic protons had a sufficient signal-to-noise ratio of the STD signals. The proton signals were calibrated to the DSS signal at 0.0 ppm. The spectra are not to scale. (**F**) MM/GBSA per-residue decomposition of the binding free energy.

pharmacophore constraints were scored using the pharmacophore fit scoring function [67].

4.2. Molecular docking calculations

Molecular docking experiments were performed with a monomer (chain A) of the human topoisomerase IIα ATPase domain (PDB: 1ZXM) [14] using the GOLD software [68]. We again followed our standardized and validated docking procedure to prepare the protein as well as the ATP binding site, which was validated in our studies on catalytic topo IIα inhibitors [22,45]. To briefly summarize, the active site was defined with a radius of 10 Å around the co-crystallized ligand AMP-PMP. Magnesium ions and crystal waters were removed, with the exception of crystal waters W924 and W931, for which a role in binding has been suggested [14]. The genetic algorithm served as the conformational search algorithm with the following settings: population size = 100, selection pressure = 1.1, number of operations = 100,000, number of islands = 5, niche size = 2, migrate = 10, mutate = 95, crossover = 95.

Different pin states of the water molecules were allowed during docking. The GoldScore scoring function was used to rank the docking solutions. The previously applied H-binding constraint was changed from Asn120 to Asn150 to slightly deprioritize the region of the adenine binding pocket in favor of the sugar and phosphate pockets [59]. The docking solutions were visualized and the binding poses were analyzed in LigandScout [67].

4.3. Molecular dynamics simulations

Protein-ligand complexes of the topo IIα ATPase domain (same PDB as in the molecular docking calculation) with compounds **1** (*Pose 1* and *Pose 2*) or compound **17** obtained by molecular docking served as starting points for molecular dynamics (MD) simulations. First, we parameterized both ligands and determined their force field parameters. The partial charges were obtained by a population analysis according to the Merz-Kollman (MK) scheme for the geometrically optimized conformations of **1** and **17**. They were optimized at the quantum mechanical Hartree-Fock (HF) level using the 6–31G(d) basis set. We used the Gaussian 16 program for these calculations [69]. The partial charges of the Restrained ElectroStatic Potential (RESP) were then generated in Antechamber module of Amber20 [70], as were the other force field parameters of the ligand, using the bond lengths and bond angles obtained from the optimized ligand geometries as input. The second generation General Amber Force Field (GAFF2) was used for the ligand description [71]. The ligand parameters of compounds **1** and **17** are available in Table S13 and S14. The topo IIα ATPase domain was prepared for simulation as in our previous studies [45]. The protein-ligand systems were solvated in TIP3P water molecules in a cubic box with a distance of at least 10 Å between the solute and the edge of the box [32]. The neutral charge of the system was achieved by adding 3 Cl^- ions. The final systems contained approximately 103,400 atoms.

The amber14SB force field was used for protein description [72] and the mentioned GAFF2 for the ligands [73]. The systems were then subjected to geometry optimization using the steepest descent method (10,000 steps), followed by conjugate gradient optimization (20,000 steps). NVT MD equilibration was performed in 4 runs, each with 10,000 steps and a time step of 2 fs, with the constraint on the protein removed gradually: the first run had a constrain 100 kcal $mol^{-1}Å^{-2}$, the second of 60 kcal $mol^{-1}Å^{-2}$, the third of 30 kcal $mol^{-1}Å^{-2}$ and the fourth was run without restraint. During NVT equilibration the systems were gently heated to reach a target temperature of 300 K, controlled by the Langevin thermostat [74]. We continued with NPT equilibration: 2 runs each 100,000 steps with time steps of 2 fs. In the first run, the ATPase domain was constrained (force constant of 20 kcal $mol^{-1}Å^{-2}$) and no constraint was applied in the second run. During NPT equilibration, the pressure was maintained at 1 bar using the Berendsen barostat [75]. The Particle Mesh Ewald method was used to treat the long-range electrostatics and periodic boundary conditions were applied [76]. The SHAKE algorithm was applied to constrain all bond lengths involving hydrogen atoms and to achieve a time step of 2 fs in all simulations [77]. A total production MD of 0.5 microseconds was performed for each of the three systems. All MD calculations were performed using the Amber20 code cuda on the Ažman computing center in Ljubljana, Slovenia [70].

Molecular trajectories were inspected and analyzed using *Cpptraj* module of Ambertools22 to calculate Root Mean Square Deviation (RMSD) [78]. MMPBSA.py. was used for the MM/GBSA binding free energy calculations [79]. Visualizations of the trajectories was performed with Visual Molecular Dynamics (VMD) [80], PyMOL [81], and UCSF Chimera software [82].

RMSD analysis (Cα atoms) was done on the whole trajectory and RMSD values were calculated referring to the initial structures of the protein and ligand complexes obtained via molecular docking with GOLD. Binding free energy calculations of the protein-ligand complex used the MM/PBSA approach [79], more precisely Generalized Born IGB method 5 (igb = 5) and 0.1 M salt concentration. Calculations were performed on equidistant 330 snapshots, leaving the first 10 ns of the MD simulation and calculating on the rest of the trajectory, thus considering only the fully equilibrated system.

Dynamical pharmacophore (dynophore) models were generated with DynophoreApp. About 2.000 equidistant frames of the equilibrated trajectory of the complexes topo IIα and bound compounds **1** (*Pose 1* and *Pose 2*) and **17** in the ATP binding site were used for obtaining each dynophore. These calculations were performed at computers of the Molecular Design Lab at Freie Universität Berlin, Germany and subsequently analyzed and visualized in LigandScout [67].

4.4. Compounds: source and characterization

Compounds **1**-**41** from the class substituted 3-(imidazol-2-yl)morpholines were obtained from the AnalytiCon Discovery, Potsdam, Germany. The structure and compound codes are available in Table S1. A representative set of active compounds was characterized *in house* by HR-MS and for key compounds **1**,**3**, **17** and **33** their purity was determined HPLC analysis to be higher than 95 % (See Supporting Information, Section 22).

4.5. Human topoisomerase IIα-mediated relaxation assay

The assays described in Subsections 4.5. to 4.9. were performed in collaboration with Inspiralis (Norwich, UK). The methodologies are standard and validated and were applied in our past studies [23,45] In all assays two independent runs were performed. Prior to testing the compounds, the activity of the topo IIα was determined, and 1 U was defined as the amount of enzyme required to fully relax the substrate. Compounds **1** and **2** were tested at concentrations of 12.5, 50, 100 and 200 μM, while all other compounds were tested at 0.781, 3.125, 12.5 and 50 μM, and were added to the reaction before the addition of the enzyme.

One U of topoisomerase IIα was incubated at 37 °C for 30 minutes with 500 ng supercoiled pBR322 in a 30 μl reaction volume containing 50 mM Tris HCl (pH 7.5), 125 mM NaCl, 10 mM $MgCl_2$, 5 mM DTT, 0.5 mM EDTA, 0.1 mg/ml bovine serum albumin (BSA) and 1 mM ATP. Final DMSO concentration in the assays was 1 % (v/v). Each reaction was stopped by the addition of 30 μl chloroform/iso-amyl alcohol (24:1) and 30 μl Stop Dye (40 % sucrose (w/v), 100 mM Tris.HCl (pH 7.5), 10 mM EDTA, 0.5 μg/ml bromophenol blue before being loaded on a 1.0 % TAE gel run at 90 V for 90 minutes. Bands were visualized by ethidium staining (15 minutes), destained in water (10 minutes) and analyzed by gel documentation equipment (Syngene, Cambridge, UK) and quantitated using Syngene Gene Tools software. Raw gel data (fluorescent band volumes) collected from Syngene, GeneTools gel analysis software were calculated as a % of the 100 % control (the fully supercoiled DNA band) and converted to % inhibition. The IC_{50} values were calculated with GraphPad Prism 9.5.0 [84].

4.6. Human topoisomerase IIβ-mediated relaxation assay

This assay was performed on compounds **1, 2**, **17**, **33**, **34**, **38** and **41** at concentrations 12.5, 50, 100 and 200 μM and for etoposide at concentrations 50 and 250 μM.

1 U of human topoisomerase IIβ was incubated with 0.5 μg of supercoiled pBR322 DNA in a 30 μl reaction volume at 37°C for 30 minutes under the following conditions: 50 mM Tris.HCl (pH 7.5), 125 mM NaCl, 10 mM MgCl2, 5 mM DTT, and 100 μg/ml albumin, 1 mM ATP and 1 % DMSO. Each reaction was stopped by extraction of the reactions with 50 μL of water saturated butan-1-ol to remove the compounds. The samples were vortexed for 10 seconds, centrifuged 30 seconds and the (upper) butanol phase was removed. The reactions were then further treated by the addition of 30 μl chloroform/iso-amyl alcohol (24:1) and 30 μl Stop Dye (40 % sucrose (w/v), 100 mM Tris. HCl (pH 7.5), 10 mM EDTA, 0.5 μg/ml bromophenol blue), before

loading 20 μL of the aqueous phase on a 1 % TAE gel. The samples were run at 90 V for 1.5 hours. Bands were visualized by ethidium bromide staining (10 minutes) and destaining (20 minutes). Gels were scanned using documentation equipment (GeneGenius, Syngene, Cambridge, UK) and % inhibition levels (where appropriate) were obtained with gel scanning software. (GeneTools, Syngene, Cambridge, UK).

4.7. Human topoisomerase IIα-mediated decatenation assay

This assay was performed for compounds **1** and **2** at concentrations 12.5, 50, 100 and 200 μM, and for etoposide at concentrations 3.9, 31.5, 125 and 500 μM. For compounds **17** and **33** the assay was performed at concentrations 0.781, 3.125, 12.5 and 50 μM, and for etoposide standard at concentrations 12.5, 50, 100 and 200 μM.

One U of topo II was incubated at 37 °C for 30 minutes with 200 ng kDNA in a 30 μL reaction volume containing: 50 mM Tris HCl (pH 7.5), 125 mM NaCl, 10 mM $MgCl_2$, 5 mM DTT, 0.5 mM EDTA, 0.1 mg/ml bovine serum albumin (BSA) and 1 mM ATP. The reaction was then stopped by the addition of 30 μl chloroform/*iso*-amyl alcohol (26:1) and 30 μL Stop Dye, before being loaded on a 1 % TAE gel run at 85 V for 90 minutes. Bands were visualized by the ethidium bromide staining (15 minutes) and destaining (10 min). Gels were scanned with the same documentation equipment (GeneGenius, Syngene, Cambridge, UK) and inhibition levels were calculated from the band raw data obtained with the gel scanning software. (GeneTools, Syngene, Cambridge, UK).

4.8. Human topoisomerase IIα cleavage and competitive cleavage assay

The cleavage assay was performed for compounds **1,2, 17,** and **33** at concentrations 12.5, 50, 100 and 200 μM and etoposide at concentrations 12.5, 50, 100 and 200 μM as control of compounds **1** and **2** and 50 and 100 μM as control of compounds **17** and **33**.

One U of the human topo IIα was incubated at 37 °C for 60 minutes with 0.5 μg supercoiled plasmid DNA (pBR322) in a 30 μL reaction volume containing 20 mM Tris HCl (pH 7.5), 200 mM NaCl, 0.25 mM EDTA and 5 % glycerol. The reaction was then incubated for a further 30 minutes with 0.2 % SDS and 0.5 μg/μL proteinase K. The reaction was then stopped by the addition of 30 μL chloroform/iso-amyl alcohol (26:1) and 30 μl Stop Dye (40 % sucrose (w/v), 100 mM Tris HCl (pH 7.5), 10 mM EDTA, 0.5 μg/ml bromophenol blue), before being loaded on a 1 % TAE gel run at 80 V for 2 hours. Bands were visualized as described in the decatenation assay.

The competitive cleavage assay was performed in duplicates for compounds **17** and **33** with the procedure described above at the same 4 concentrations as above, with the difference that a constant etoposide concentration of 50 μM of etoposide was also present. The amount of etoposide required for optimal cleavage was determined by prior titration. Total DMSO in the assay was 2 % (cumulative effect of adding 2 different compounds).

4.9. Wheatgerm topo I unwinding Assay

This assay was performed for compounds **1, 2**, **17**, and **33** at concentrations 12.5, 50, 100 and 200 μM, and mAMSA was added as a control at concentrations 12.5, 50, 100 and 200 μM.

Compounds were incubated at 37°C for 30 minutes with an excess of wheatgerm topo I and 0.5 μg supercoiled plasmid DNA in a 30 μL reaction volume containing 50 mM Tris-HCl (pH 7.9), 50 mM NaCl, 1.0 mM EDTA, 1.0 mM DTT, 20 % (v/v) glycerol. Compounds were diluted from 50 mM stocks in 100 % DMSO. Each reaction was stopped, and the compounds removed prior to running of the gels by the addition of 50 μl butanol and 30 μl of water, the samples vortexed and the aqueous layer removed before the addition of 30 μl chloroform/iso-amyl alcohol (24:1) and 30 μl Stop Dye. These were then loaded on a 1.0 % TAE gel run at 90 V for 2 hours. Bands were visualized by ethidium bromide staining (15 minutes) and destaining (10 minutes). Gels were scanned using documentation equipment (GeneGenius, Syngene, Cambridge, UK).

4.10. STD NMR spectroscopy experiments

STD NMR experiments were recorded on a Bruker Avance Neo 600 MHz spectrometer with a cryoprobe at 25°C using the pulse sequences included in the Bruker TopSpin library of pulse programs. Samples contained 2 μM of the ATPase domain of topo IIα (purchased from Inspiralis, UK) in a 20 mM K-phosphate (pD 7.7) buffer containing 150 mM KCl, 5 mM $MgCl_2$, and 0.02 % NaN_3 dissolved in D_2O. The ligands were dissolved in DMSO-d_6 and added to the samples at a ligand: protein ratio of 100:1. The final concentration of DMSO-d_6 in the samples was 10 %.

The ^{1}H 1D STD ligand epitope mapping experiments [85] spectra of compounds **17** and **33** were acquired with a spectral width of 5882 Hz, 32,768 data points, a relaxation delay of 3 s, and 3520 scans. For compound **1,** 65,536 data points and a relaxation delay of 1.5 s were used. The on-resonance selective saturation of TOPOII was applied for 1 s at −0.725 ppm with a transmitter offset referenced to 4.702 ppm. The off-resonance irradiation was applied at 30 ppm for the reference spectrum. The residual water signal was suppressed by excitation-sculpting with 2 ms selective pulse and a $T_1\rho$ filter of 100 ms was used to eliminate background protein resonances. The spectra were zero-filled twice and apodized with an exponential line-broadening function of 3 and 5 Hz in the case of compound **1** with a lower signal-to-noise ratio of the STD spectrum compared to compounds **17** and **33**.

4.11. Inhibition assays of human protein kinases

Inhibition assays of compounds **1** and **17** on a selected set of human protein kinases were performed with *KinaseProfiler™* service (Eurofins Cerep SA, Celle-L'Evescault, France) using their developed KinaseProfiler kinase activity radiometric assays. Both compounds were first prepared to the 50x final assay concentration in 100 % DMSO. This working stock of each compound was added to the assay well as the first component in the reaction, followed by the remaining components as detailed in the general assay protocols below (Table 4).

In the standard *KinaseProfiler™* service there is no pre-incubation step between the compound and the kinase prior to initiation of the reaction. The positive control wells contained all components of the reaction, except the compound of interest; however, DMSO at a final concentration of 2 % was included in these wells to control for solvent effects. The blank wells contained all components of the reaction, with a reference kinase inhibitor replacing the compound of interest. This abolishes kinase activity and establishes the base-line (0 % kinase activity remaining). Table 5 lists the reference inhibitors used to generate the blank signal for each tested protein kinase. The listed kinase

Table 4
Specific buffer compositions utilized for the preparation of tested protein kinases before their addition to the reaction mix.

Buffer Composition	Protein Kinase(s)
20 mM MOPS, 1 mM EDTA, 0.01 % Brij-35, 5 % Glycerol, 0.1 % β- mercaptoethanol, 1 mg/ml BSA	CDK1/cyclinB, c-Kit, EGFR, FGFR1, FGFR3, Flt1, Flt3, Fms, JAK2, PDGFRα, PKA, PKBα, Ret, Src (1−530)
45 mM TRIS, 0.4 mM EGTA, 18 mM DTT, 0.02 % Triton X-100, 1 mM sodium orthovandate, 1 mM β-glycerophosphate, 2 % glycerol	B-Raf, c-Raf
50 mM TRIS, 0.1 mM EGTA, 0.1 mM Na3VO4, 0.1 % β- mercaptoethanol, 1 mg/ml BSA	IGF-1R
50 mM HEPES, 1 mM EDTA, 10 mM DTT, 0.01 % Brij-35	MEKK3

Table 5
Selection of reference kinase inhibitors and their target protein kinases:.

Reference kinase Inhibitor	Protein Kinase(s)
PI-103	DNA-PK
KU55933	ATM
Staurosporine	B-Raf, CDK1/cyclinB, cKit, c-Raf, EGFR, FGFR1, FGFR3, Flt1, Flt3, Fms, IGF-1R, JAK2, MEKK3, PDGFRα, PKA, PKBα, Ret, Src(1−530)

inhibitors were chosen as references and added at concentrations known to achieve complete inhibition, contributing to the creation of blank wells in the experimental setup. All experiments were performed in duplicates. Exact assay protocols that were used to evaluate inhibition activity of each selected protein kinase are described in detail in Supplementary information, Section 16.

4.12. Experiments on cancer cell lines

4.12.1. Cell culture

Hepatocellular carcinoma (HepG2; ATCC-HB-8065™) and breast cancer (MCF-7; ATCC-HTB-22™) cell lines were used to evaluate cytotoxic activity of the studied compounds. HepG2 cells were cultured in minimum essential medium Eagle (MEME) (MEME-10370–047), containing NEAA supplemented with 10 % foetal bovine serum (FBS), 2.2 g/L NaHCO3, 1 mM sodium pyruvate, 2 mM L-Glutamine, and 100 IU/ml penicillin/streptomycin (all from Sigma, St. Louis MO, USA). MCF-7 cells were cultured in Eagle's minimum essential medium (MEM; M5650), supplemented with 10 % FBS, 0.01 mg/ml insulin, 2 mM glutamine, and 100 IU/ml penicillin/streptomycin (all from Sigma, St. Louis MO, USA). Both cell lines were cultured at 37 °C in humidified atmosphere with 5 % CO2.

4.12.2. Determination of cytotoxic activity by MTS assay

The viability of HepG2 and MCF-7 cells after 24 and 72 h exposure to selected compounds was determined by the tetrazolium-based (MTS; 3-(4,5-dimethylthiazol-2-yl)-5-(3-carboxymethoxyphenyl)-2-(4-sulfophenyl)-2 H-tetrazolium) assay (Cell Titer 96 AQueous Non-Radioactive Cell Proliferation Assay; Promega, Madison, WI, USA). Briefly, HepG2 and MCF-7 cells were seeded in 96-well microtiter plates (Nunc, Thermo Fisher Scientific, Waltham, MA) at a density of 8000 and 6000 cells/well for 24 hours and 4000 and 6000 cells/well for 72 hours of treatment, respectively. After 24 hours, the culture medium was replaced with fresh medium containing the following concentrations of tested compounds **10**, **13**, **17, 28**, **33**, **34**, and **35;** 5, 100, 200, 400 μM for 24 h and 25, 50, 100 and 200 μM for 72 h, while compound **17** was tested at 12.5, 25, 50, 100 μM for 24 hours and 6.25, 12.5, 25, 100 μM for 72 hours. In addition, etoposide reference was tested at 100, 200, 300, and 400 μM for 24 hours and 5, 25, 50, and 100 μM for 72 hours, respectively.

After incubation, 40 μL of the MTS /PMS (20:1) mixture was added to each well containing 200 μL medium for 3 h (37 °C, 5 % CO_2), and then the absorbance was measured at 490 nm using a Synergy MX spectrofluorometer (BioTek, Winooski, VT, USA). Cell viability is expressed as the percentage of the solvent control at each exposure time point. Three independent experiments were performed each time with five replicates per treatment time point. Statistical significance between the control and treated groups was determined by one-way analysis of variance and Dunnett's multiple comparison test, and EC_{50} values were calculated by non-linear regression analysis using GraphPad Prism v6.00 [86].

4.12.3. Measurements of cell proliferation, cell cycle progression, and γ-H2AX expression by flow cytometry

HepG2 and MCF-7 cells were seeded on 25 cm^2 plates (Corning Inc, NY) at a density of 750,000 or 400,000 cells/plate and 400,000 or 250,000 cells/plate for 24 hour and 72 hours of exposure, respectively, to selected compound and allowed to adhere overnight. The next day, cells were treated with compound **17** at concentrations of 12.5, 25, and 50 μM for 24 hours and 6.25, 12.5, 25, and 50 μM for 72 hours. 100 and 50 μM etoposide was used as a positive control for 24 and 72 hours, respectively. After treatment, cells were collected, fixed in 75 % ethanol, and labelled with anti-H2AX pS139 (Miltenyi Biotech, Germany) antibody for DNA DSB analysis, anti-Ki67 antibody (Miltenyi Biotech, Germany) for cell proliferation analysis, and Hoechst 33342 dye for cell cycle analysis as previously described [23]. For each sample, 15.000 events were acquired using a flow cytometer MACSQuant Analyzer 10 with MACSQuantify™ software (Miltenyi Biotech, Germany). For analysis of results, raw data were exported from MACSQuantify software and analyzed with FlowJo V10 software (Becton Dickinson, New Jersey USA).

Statistically significant differences between cells exposed to compound **17** and control samples in the % of Ki67-positive cells were determined by one-way ANOVA with Dunnett's multiple comparison test and statistically significant difference in APC fluorescence (γH2AX) was determined by two-way ANOVA with Uncorrected Fisher's LSD using GraphPad Software V6 [86]. Cell cycle distribution was evaluated with the univariate Dean–Jett–Fox cell cycle model on single, debris-free cells and statistical significance in the cell-cycle distributions was determined using the chi-square test using GraphPad Software V6. Statistical significance was defined as $p \leq 0.05$.

4.12.4. NCI-60 human tumor cell lines screen

The compounds **1**, **17** and **33** were assayed by the National Cancer Institute (NCI, USA) on a panel of 60 human cancer cell lines. A list of the assayed cell lines is available on the NCI website and the testing method involved fixing the cells with trichloroacetic acid, followed by staining with sulforhodamine B (SRB) and absorbance measurement [87–89]. Compounds were tested at a concentration of 10 μM and the NCS codes for the assays are *842914* (compound **1**), *842912* (compound **17**), and *842913* (compound **33**). Results are reported as growth values relative to the control without compound and relative to the number of cells at time zero. Thus, we were able to determine no growth inhibition (values between 0 and 100) and lethality (values between −100 and 0) [88].

CRediT authorship contribution statement

Barbara Herlah: Writing – review & editing, Writing – original draft, Visualization, Investigation. **Matej Janežič:** Writing – review & editing, Writing – original draft, Visualization, Investigation. **Iza Ogris:** Visualization, Investigation. **Simona Golič Grdadolnik:** Visualization, Investigation. **Katja Kološa:** Visualization, Investigation. **Sonja Žabkar:** Visualization, Investigation. **Bojana Žegura:** Visualization, Investigation. **Andrej Perdih:** Writing – review & editing, Writing – original draft, Supervision, Investigation, Funding acquisition, Conceptualization.

Declaration of Competing Interest

The authors declare that they have no known competing financial interests or personal relationships that could have appeared to influence the work reported in this paper.

Acknowledgment

This work was supported by the Slovenian Research and Innovation Agency (ARIS) through research projects J1-4402 (A.P.) and J1-4400 (S. G.G) and research programs P1–0012, P1–0010 and P1–0245 and a young researcher funding to B.H and I.O. Dr. Nicolas Burton and Dr. Alison Howells from Inspiralis, Norwich, UK are acknowledged for expressing and isolating the ATPase domain of human topo IIα as well as performing topoisomerase IIα relaxation, decatenation, cleavage,

competitive cleavage and unwinding assays. Dr. Kaja Bergant Loboda from the National Institute of Chemistry is acknowledged for assistance with initial inhibition assays of hit compounds. Dr. Lars Ole Haustedt and AnalytiCon Discovery, Potsdam, Germany are sincerely thanked for providing us with the hit compounds **1** and **2** from their chemical libraries in the initial stage of this work. Prof. Gerhard Wolber is thanked for providing us access to dynophore calculations at the computer cluster of the Freie Universität Berlin, Germany. We recorded NMR spectra on NMR spectrometers of Slovenian NMR Centre at National Institute of Chemistry, Ljubljana. We acknowledge Ažman high-performance computing (HPC) center at the National Institute of Chemistry in Ljubljana for computational resources and National Cancer Institute (NCI), USA for accepting our compounds to be assayed within their NCI-60 program.

Supplementary material

Supplementary Information includes: (1) Supporting figures, tables, and graphs (pdf file), (2) Coordinates of the topo IIα ATPase protein (monomer A) and the docked compounds **1** (*Pose 1* and *Pose 2*) and **17** used as starting points for molecular simulation (zip file), (3) Animation 1: Derived dynamical pharmacophore models of hit compound **1** and compound **17** depicted on the obtained MD trajectory (mp4 file).

Appendix A. Supporting information

Supplementary data associated with this article can be found in the online version at doi:10.1016/j.biopha.2024.116676.

References

[1] Y. Pommier, Y. Sun, S.N. Huang, J.L. Nitiss, Roles of eukaryotic topoisomerases in transcription, replication and genomic stability, Nat. Rev. Mol. Cell Biol. 17 (2016) 703–721.
[2] S.M. Vos, E.M. Tretter, B.H. Schmidt, J.M. Berger, All tangled up: how cells direct, manage and exploit topoisomerase function, Nat. Rev. Mol. Cell Biol. 12 (2011) 827–841.
[3] A.D. Bates, A. Maxwell, DNA topology: topoisomerases keep it simple, Curr. Biol. 7 (1997) R778–R781.
[4] J.J. Champoux, DNA topoisomerases: structure, function, and mechanism, Ann. Rev. Biochem. 70 (2001) 369–413.
[5] M. Pavlin, B. Herlah, K. Valjavec, A. Perdih, Unveiling the interdomain dynamics of type II DNA topoisomerase through all-atom simulations: Implications for understanding its catalytic cycle, Comput. Struct. Biotechnol. J. 21 (2023) 3746–3759.
[6] M. Ogrizek, M. Janežič, K. Valjavec, A. Perdih, Catalytic Mechanism of ATP hydrolysis in the ATPase domain of human DNA topoisomerase IIα, J. Chem. Inf. Model 62 (2022) 3896–3909.
[7] M. Watanabe, K. Tsutsui, K. Tsutsui, Y. Inoue, Differential expressions of the topoisomerase IIα and IIβ mRNAs in developing rat brain, Neurosci. Res. 19 (1994) 51–57.
[8] G. Capranico, S. Tinelli, C.A. Austin, M.L. Fisher, F. Zunino, Different patterns of gene expression of topoisomerase II isoforms in differentiated tissues during murine development, Biochim. Biophys. Acta 1132 (1992) 43–48.
[9] A.K. McClendon, N. Osheroff, DNA topoisomerase II, genotoxicity, and cancer, Mutat. Res. 623 (2007) 83–97.
[10] A. Sakaguchi, A. Kikuchi, Functional compatibility between isoform α and β of type II DNA topoisomerase, J. Cell Sci. 117 (2004) 1047–1054.
[11] P. Chene, J. Rudloff, J. Schoepfer, P. Furet, P. Meier, Z. Qian, J.M. Schlaeppi, R. Schmitz, T. Radimerski, Catalytic inhibition of topoisomerase II by a novel rationally designed ATP-competitive purine analogue, BMC Chem. Biol. 9 (2009) 1.
[12] V. Vidmar, M. Vayssieres, V. Lamour, What's on the other side of the gate: a structural perspective on DNA gate opening of type IA and IIA DNA topoisomerases, Int. J. Mol. Sci. 24 (2023).
[13] B.H. Schmidt, N. Osheroff, J.M. Berger, Structure of a topoisomerase II-DNA-nucleotide complex reveals a new control mechanism for ATPase activity, Nat. Struct. Mol. Biol. 19 (2012) 1147–1154.
[14] H. Wei, A.J. Ruthenburg, S.K. Bechis, G.L. Verdine, Nucleotide-dependent domain movement in the ATPase domain of a human type IIA DNA topoisomerase, J. Biol. Chem. 280 (2005) 37041–37047.
[15] F.V. Stanger, C. Dehio, T. Schirmer, Structure of the N-terminal Gyrase B fragment in complex with ADP·Pi reveals rigid-body motion induced by ATP hydrolysis, PLoS One 9 (2014) e107289.
[16] A. Vanden Broeck, C. Lotz, R. Drillien, L. Haas, C. Bedez, V. Lamour, Structural basis for allosteric regulation of Human Topoisomerase IIα, Nat. Commun. 12 (2021) 2962.
[17] J.L. Nitiss, Targeting DNA topoisomerase II in cancer chemotherapy, Nat. Rev. Cancer 9 (2009) 338–350.
[18] B. Pogorelčnik, A. Perdih, T. Solmajer, Recent developments of DNA poisons - human DNA topoisomerase IIα inhibitors - as anticancer agents, Curr. Pharm. Des. 19 (2013) 2474–2488.
[19] B. Pogorelčnik, A. Perdih, T. Solmajer, Recent advances in the development of catalytic inhibitors of human DNA topoisomerase IIα as novel anticancer agents, Curr. Med. Chem. 20 (2013) 694–709.
[20] G. Minotti, P. Menna, E. Salvatorelli, G. Cairo, L. Gianni, Anthracyclines: Molecular advances and pharmacologic developments in antitumor activity and cardiotoxicity, Pharmacol. Rev. 56 (2004) 185–229.
[21] C.A. Felix, Secondary leukemias induced by topoisomerase-targeted drugs, Biochim Biophys. Acta 1400 (1998) 233–255.
[22] K. Bergant, M. Janežic, K. Valjavec, I. Sosič, S. Pajk, M. Štampar, B. Žegura, S. Gobec, M. Filipič, A. Perdih, Structure-guided optimization of 4,6-substituted-1,3,5-triazin-2(1H)-ones as catalytic inhibitors of human DNA topoisomerase IIα, Eur. J. Med. Chem. 175 (2019) 330–348.
[23] K. Bergant Loboda, M. Janežič, M. Štampar, B. Žegura, M. Filipič, A. Perdih, Substituted 4,5′-bithiazoles as catalytic inhibitors of human DNA topoisomerase IIα, J. Chem. Inf. Model 60 (2020) 3662–3678.
[24] K.B. Loboda, K. Valjavec, M. Štampar, G. Wolber, B. Žegura, M. Filipič, M. S. Dolenc, A. Perdih, Design and synthesis of 3,5-substituted 1,2,4-oxadiazoles as catalytic inhibitors of human DNA topoisomerase IIα, Bioorg. Chem. 99 (2020) 103828.
[25] L. Pinzi, G. Rastelli, Molecular docking: shifting paradigms in drug discovery, Int. J. Mol. Sci. 20 (2019).
[26] S.S. Bhunia, M. Saxena, A.K. Saxena, Ligand- and structure-based virtual screening in drug discovery, in: A.K. Saxena (Ed.), Biophysical and Computational Tools in Drug Discovery, Springer International Publishing, Cham, 2021, pp. 281–339.
[27] D. Schaller, D. Šribar, T. Noonan, L. Deng, T.N. Nguyen, S. Pach, D. Machalz, M. Bermudez, G. Wolber, Next generation 3D pharmacophore modeling, WIREs Comput. Mol. Sci. 10 (2020) e1468.
[28] A. Fischer, M. Smieško, M. Sellner, M.A. Lill, Decision making in structure-based drug discovery: visual inspection of docking results, J. Med Chem. 64 (2021) 2489–2500.
[29] D. Gioia, M. Bertazzo, M. Recanatini, M. Masetti, A. Cavalli, Dynamic docking: a paradigm shift in computational drug discovery, Molecules 22 (2017).
[30] R. Buonfiglio, M. Recanatini, M. Masetti, Protein flexibility in drug discovery: from theory to computation, Chem. Med. Chem. 10 (2015) 1141–1148.
[31] V. Salmaso, S. Moro, Bridging molecular docking to molecular dynamics in exploring ligand-protein recognition process: an overview, Front. Pharmacol. 9 (2018) 923.
[32] W. Jorgensen, J. Chandrasekhar, J. Madura, R. Impey, M. Klein, Comparison of simple potential functions for simulating liquid water, J. Chem. Phys. 79 (1983) 926–935.
[33] M. De Vivo, M. Masetti, G. Bottegoni, A. Cavalli, Role of molecular dynamics and related methods in drug discovery, J. Med. Chem. 59 (2016) 4035–4061.
[34] L. Katz, R.H. Baltz, Natural product discovery: past, present, and future, J. Ind. Microbiol Biotechnol. 43 (2016) 155–176.
[35] A.G. Atanasov, S.B. Zotchev, V.M. Dirsch, , T. International Natural Product Sciences, C.T. Supuran, Natural products in drug discovery: advances and opportunities, Nat. Rev. Drug Discov. 20 (2021) 200–216.
[36] J. Mann, Natural products in cancer chemotherapy: past, present and future, Nat. Rev. Cancer 2 (2002) 143–148.
[37] Y. Chen, C. de Bruyn Kops, J. Kirchmair, Data resources for the computer-guided discovery of bioactive natural products, J. Chem. Inf. Model 57 (2017) 2099–2111.
[38] D.J. Newman, G.M. Cragg, Natural Products as Sources of New Drugs over the Nearly Four Decades from 01/1981 to 09/2019, J. Nat. Prod. 83 (2020) 770–803.
[39] J. Hong, Role of natural product diversity in chemical biology, Curr. Opin. Chem. Biol. 15 (2011) 350–354.
[40] F.E. Koehn, G.T. Carter, The evolving role of natural products in drug discovery, Nat. Rev. Drug Discov. 4 (2005) 206–220.
[41] L.O. Haustedt, C. Mang, K. Siems, H. Schiewe, Rational approaches to natural-product-based drug design, Curr. Opin. Drug Discov. Dev. 9 (2006) 445–462.
[42] A.L. Harvey, Natural products in drug discovery, Drug Discov. Today 13 (2008) 894–901.
[43] A.L. Harvey, R. Edrada-Ebel, R.J. Quinn, The re-emergence of natural products for drug discovery in the genomics era, Nat. Rev. Drug Discov. 14 (2015) 111–129.
[44] L. Laraia, H. Waldmann, Natural product inspired compound collections: evolutionary principle, chemical synthesis, phenotypic screening, and target identification, Drug Discov. Today Technol. 23 (2017) 75–82.
[45] M. Janežič, K. Valjavec, K.B. Loboda, B. Herlah, I. Ogris, M. Kozorog, M. Podobnik, S.G. Grdadolnik, G. Wolber, A. Perdih, Dynophore-based approach in virtual screening: a case of human DNA topoisomerase IIα, Int. J. Mol. Sci. 22 (2021) 13474.
[46] O.J. Bandele, N. Osheroff, Bioflavonoids as poisons of human topoisomerase IIα and IIβ, Biochemistry 46 (2007) 6097–6108.
[47] N. Patra, U. De, J.A. Kang, J.M. Kim, M.Y. Ahn, J. Lee, J.H. Jung, H.Y. Chung, H. R. Moon, H.S. Kim, A novel epoxypropoxy flavonoid derivative and topoisomerase II inhibitor, MHY336, induces apoptosis in prostate cancer cells, Eur. J. Pharmacol. 658 (2011) 98–107.
[48] W. Tian, C. Chen, X. Lei, J. Zhao, J. Liang, CASTp 3.0: computed atlas of surface topography of proteins, Nucleic Acids Res. 46 (2018) W363–W367.
[49] R. Dutta, M. Inouye, GHKL, an emergent ATPase/kinase superfamily, Trends Biochem Sci. 25 (2000) 24–28.

[50] P. Chene, ATPases as drug targets: Learning from their structure, Nat. Rev. Drug Discov. 1 (2002) 665–673.
[51] AnalytiCon Discovery, Personal communication. 2023.
[52] C. Wang, D. Greene, L. Xiao, R. Qi, R. Luo, Recent Developments and Applications of the MMPBSA Method, Front. Mol. Biosci. 4 (2017) 87.
[53] J.T. Bau, Z. Kang, C.A. Austin, E.U. Kurz, Salicylate, a catalytic inhibitor of topoisomerase II, inhibits DNA cleavage and is selective for the α isoform, Mol. Pharm. 85 (2014) 198–207.
[54] F. Gao, H. Chao, F. Zhou, X. Chen, Y.F. Wei, L.N. Ji, Synthesis, GC selective DNA binding and topoisomerase II inhibition activities of ruthenium(II) polypyridyl complex containing 11-aminopteridino[6,7-f][1,10]phenanthrolin-13(12H)-one, J. Inorg. Biochem 102 (2008) 1050–1059.
[55] M.Y. Liu, W.Z. Wang, F.F. Liao, Q.Q. Wu, X.H. Lin, Y.H. Chen, L. Cheng, X.B. Jin, J. Y. Zhu, Selective and effective targeting of chronic myeloid leukemia stem cells by topoisomerase II inhibitor etoposide in combination with imatinib mesylate in vitro, Cell Biol. Int. 41 (2017) 16–23.
[56] J.A. Ortega, J.M. Arencibia, E. Minniti, J.A.W. Byl, S. Franco-Ulloa, M. Borgogno, V. Genna, M. Summa, S.M. Bertozzi, R. Bertorelli, A. Armirotti, A. Minarini, C. Sissi, N. Osheroff, M. De Vivo, Novel, Potent, and Druglike Tetrahydroquinazoline Inhibitor That Is Highly Selective for Human Topoisomerase II α over β, J. Med. Chem. 63 (2020) 12873–12886.
[57] E. Toyoda, S. Kagaya, I.G. Cowell, A. Kurosawa, K. Kamoshita, K. Nishikawa, S. Iiizumi, H. Koyama, C.A. Austin, N. Adachi, NK314, a topoisomerase II inhibitor that specifically targets the α isoform, J. Biol. Chem. 283 (2008) 23711–23720.
[58] K. Bergant, M. Janežič, A. Perdih, Bioassays and in silico methods in the identification of human DNA topoisomerase IIα inhibitors, Curr. Med Chem. 25 (2018) 3286–3318.
[59] B. Pogorelčnik, M. Brvar, B. Žegura, M. Filipič, T. Solmajer, A. Perdih, Discovery of mono- and disubstituted 1*H*-pyrazolo[3,4]pyrimidines and 9*H*-purines as catalytic inhibitors of human DNA topoisomerase IIα, Chem. Med. Chem. 10 (2015) 345–359.
[60] A. Alpsoy, S. Yasa, U. Gunduz, Etoposide resistance in MCF-7 breast cancer cell line is marked by multiple mechanisms, Biomed. Pharmacother. 68 (2014) 351–355.
[61] The Human Protein Atlas, ⟨https://www.proteinatlas.org/ENSG00000131747-TOP2A/tissue⟩, 31. 01. 2024.
[62] Human Proteome Map, ⟨https://www.humanproteomemap.org⟩, 23. 10. 2023.
[63] J.M. Henwood, R.N. Brogden, Etoposide. A review of its pharmacodynamic and pharmacokinetic properties, and therapeutic potential in combination chemotherapy of cancer, Drugs 39 (1990) 438–490.
[64] D.J. Smart, H.D. Halicka, G. Schmuck, F. Traganos, Z. Darzynkiewicz, G. M. Williams, Assessment of DNA double-strand breaks and gammaH2AX induced by the topoisomerase II poisons etoposide and mitoxantrone, Mutat. Res 641 (2008) 43–47.
[65] Ž. Skok, N. Zidar, D. Kikelj, J. Ilaš, Dual inhibitors of human DNA topoisomerase II and other cancer-related targets, J. Med Chem. (2019).
[66] AnalytiCon Discovery, ⟨https://ac-discovery.com/synthetic-screening-compounds⟩, 19. 1. 2024.
[67] G. Wolber, T. Langer, LigandScout: 3-D pharmacophores derived from protein-bound ligands and their use as virtual screening filters, J. Chem. Inf. Model. 45 (2005) 160–169.
[68] G. Jones, P. Willett, R.C. Glen, A.R. Leach, R. Taylor, Development and validation of a genetic algorithm for flexible docking, J. Mol. Biol. 267 (1997) 727–748.
[69] M.J. Frisch, G.W. Trucks, H.B. Schlegel, G.E. Scuseria, M.A. Robb, J.R. Cheeseman, G. Scalmani, V. Barone, G.A. Petersson, H. Nakatsuji, X. Li, M. Caricato, A.V. Marenich, J. Bloino, B.G. Janesko, R. Gomperts, B. Mennucci, H.P. Hratchian, J.V. Ortiz, A.F. Izmaylov, J.L. Sonnenberg, Williams, F. Ding, F. Lipparini, F. Egidi, J. Goings, B. Peng, A. Petrone, T. Henderson, D. Ranasinghe, V.G. Zakrzewski, J. Gao, N. Rega, G. Zheng, W. Liang, M. Hada, M. Ehara, K. Toyota, R. Fukuda, J. Hasegawa, M. Ishida, T. Nakajima, Y. Honda, O. Kitao, H. Nakai, T. Vreven, K. Throssell, J.A. Montgomery Jr, J.E. Peralta, F. Ogliaro, M.J. Bearpark, J.J. Heyd, E. N. Brothers, K.N. Kudin, V.N. Staroverov, T.A. Keith, R. Kobayashi, J. Normand, K. Raghavachari, A.P. Rendell, J.C. Burant, S.S. Iyengar, J. Tomasi, M. Cossi, J.M. Millam, M. Klene, C. Adamo, R. Cammi, J.W. Ochterski, R.L. Martin, K. Morokuma, O. Farkas, J.B. Foresman, D.J. Fox, Gaussian 16 Rev. C.01, in, Wallingford, CT, 2016.
[70] D.A. Case, K. Belfon, I.Y. Ben-Shalom, S.R. Brozell, D.S. Cerutti, I.T.E. Cheatham, V. W.D. Cruzeiro, T.A. Darden, R.E. Duke, G. Giambasu, M.K. Gilson, H. Gohlke, A.W. Goetz, R. Harris, S. Izadi, S.A. Izmailov, K. Kasavajhala, A. Kovalenko, R. Krasny, T. Kurtzman, T.S. Lee, S. LeGrand, P. Li, C. Lin, J. Liu, T. Luchko, R. Luo, V. Man, K.M. Merz, Y. Miao, O. Mikhailovskii, G. Monard, H. Nguyen, A. Onufriev, F.Pan, S. Pantano, R. Qi, D.R. Roe, A. Roitberg, C. Sagui, S. Schott-Verdugo, J. Shen, C.L. Simmerling, N.R.Skrynnikov, J. Smith, J. Swails, R.C. Walker, J. Wang, L. Wilson, R.M. Wolf, X. Wu, Y. Xiong, Y. Xue, D.M. York, P.A. Kollman, AMBER 2020, in, University of California, San Francisco, 2020.
[71] X. He, V.H. Man, W. Yang, T.S. Lee, J. Wang, A fast and high-quality charge model for the next generation general AMBER force field, J. Chem. Phys. 153 (2020) 114502.
[72] J.A. Maier, C. Martinez, K. Kasavajhala, L. Wickstrom, K.E. Hauser, C. Simmerling, ff14SB: Improving the accuracy of protein side chain and backbone parameters from ff99SB, J. Chem. Theory Comput. 11 (2015) 3696–3713.
[73] J. Wang, R.M. Wolf, J.W. Caldwell, P.A. Kollman, D.A. Case, Development and testing of a general amber force field, J. Comput. Chem. 25 (2004) 1157–1174.
[74] G.S. Grest, K. Kremer, Molecular dynamics simulation for polymers in the presence of a heat bath, Phys. Rev. A Gen. Phys. 33 (1986) 3628–3631.
[75] H.J.C. Berendsen, J.P.M. Postma, W.F. van Gunsteren, A. DiNola, J.R. Haak, Molecular dynamics with coupling to an external bath, J. Chem. Phys. 81 (1984) 3684–3690.
[76] T. Darden, D. York, L. Pedersen, Particle mesh Ewald: An N·log(N) method for Ewald sums in large systems, J. Chem. Phys. 98 (1993) 10089–10092.
[77] J.-P. Ryckaert, G. Ciccotti, H.J.C. Berendsen, Numerical integration of the cartesian equations of motion of a system with constraints: molecular dynamics of n-alkanes, J. Comput. Phys. 23 (1977) 327–341.
[78] D.A. Case, H.M. Aktulga, K. Belfon, I.Y. Ben-Shalom, J.T. Berryman, S.R. Brozell, D. S. Cerutti, I.T.E. Cheatham, G.A. Cisneros, V.W.D. Cruzeiro, T.A. Darden, N. Forouzesh, G. Giambaşu, T. Giese, M.K. Gilson, H. Gohlke, A.W. Goetz, J. Harris, S. Izadi, S.A. Izmailov, K. Kasavajhala, M.C. Kaymak, E. King, A. Kovalenko, T. Kurtzman, T.S. Lee, P. Li, C. Lin, J. Liu, T. Luchko, R. Luo, M. Machado, V. Man, M. Manathunga, K.M. Merz, Y. Miao, O. Mikhailovskii, G. Monard, H. Nguyen, K. A. O'Hearn, A. Onufriev, S.P.F. Pan, A.R.R. Qi, D.R. Roe, A. Roitberg, C. Sagui, S. Schott-Verdugo, A. Shajan, J. Shen, C.L. Simmerling, N.R. Skrynnikov, J. Smith, J. Swails, R.C. Walker, J. Wang, J. Wang, H. Wei, X. Wu, Y. Wu, Y. Xiong, Y. Xue, D.M. York, S. Zhao, Q. Zhu, P.A. Kollman. AMBER 2022, in, University of California, San Francisco, 2022.
[79] B.R. Miller III, T.D. McGee, Jr, J.M. Swails, N. Homeyer, H. Gohlke, A.E. Roitberg, MMPBSA.py: an efficient program for end-state free energy calculations, J. Chem. Theory Comput. 8 (2012) 3314–3321.
[80] W. Humphrey, A. Dalke, K. Schulten, VMD: Visual molecular dynamics, J. Mol. Graph Model 14 (1996) 33–38.
[81] L. Schrodinger, PyMOL Mol. Graph. Syst. (2015).
[82] E.F. Pettersen, T.D. Goddard, C.C. Huang, G.S. Couch, D.M. Greenblatt, E.C. Meng, T.E. Ferrin, UCSF Chimera-A visualization system for exploratory research and analysis, J. Comput. Chem. 25 (2004) 1605–1612.
[83] B. Pogorelčnik, M. Janežič, I. Sosič, S. Gobec, T. Solmajer, A. Perdih, 4,6-Substituted-1,3,5-triazin-2(1H)-ones as monocyclic catalytic inhibitors of human DNA topoisomerase IIα targeting the ATP binding site, Bioorg. Med Chem. 23 (2015) 4218–4229.
[84] GraphPad Software, GraphPad Prism Version 9 for Windows, ⟨www.graphpad.com⟩, 6. 1. 2024.
[85] M. Mayer, B. Meyer, Group epitope mapping by saturation transfer difference NMR to identify segments of a ligand in direct contact with a protein receptor, J. Am. Chem. Soc. 123 (2001) 6108–6117.
[86] GraphPad Software, GraphPad Prism Version 6 for Windows, ⟨www.graphpad.com⟩, 15. 10. 2023.
[87] NCI-60 Cell Lines in the In Vitro Screen, ⟨https://dtp.cancer.gov/discovery_development/nci-60/cell_list.htm⟩, 11. 07. 2023.
[88] NCI-60 Screening Methodology, ⟨https://dtp.cancer.gov/discovery_development/nci-60/methodology.htm⟩, 11. 07. 2023.
[89] R.H. Shoemaker, The NCI60 human tumour cell line anticancer drug screen, Nat. Rev. Cancer 6 (2006) 813–823.